

VRIJE  
UNIVERSITEIT  
BRUSSEL

<sup>1</sup> **A search for flavour changing neutral currents  
2 involving a top quark and a Z boson, using the  
3 data collected by the CMS collaboration at a  
4 centre of mass of 13 TeV**

<sup>5</sup> Van Parijs, Isis

<sup>6</sup> Proefschrift ingediend met het oog op het behalen van de academische graad  
<sup>7</sup> Doctor in de Wetenschappen.

Published in Faculteit Wetenschappen & Bio-ingenieurswetenschappen  
Vrije Universiteit Brussel  
At 1. June 2017.

<sup>8</sup>

Responsible Contact: I. Van Parijs  
Institute for High Energy Physics  
Promotor: Prof. Jorgen D'Hondt

First Referee: Prof. Dr. J. D'Hondt

9 Date of Hand-in:

Date of Defense: 10 December 2017

# Contents

---

11	<b>1 An introduction to the theory</b>	1
12	1.1 Elementary particles and forces . . . . .	1
13	1.2 Standard Model Lagrangian . . . . .	3
14	1.3 Flavour changing currents in the SM . . . . .	5
15	1.4 Motivations for new physics . . . . .	6
16	1.5 An effective approach beyond the SM: FCNC involving a top quark . . . . .	8
17	1.6 Experimental constraints on top-FCNC . . . . .	9
18	1.7 Statistics for a high energy particle physicist . . . . .	10
19	1.7.1 Boosted decision trees . . . . .	10
20	1.7.2 Confidence levels . . . . .	10
21	1.7.3 Combine limit setting tool . . . . .	10
22	<b>2 Experimental set-up</b>	13
23	2.1 The Large Hadron Collider . . . . .	13
24	2.1.1 LHC design and operation . . . . .	15
25	2.2 The Compact Muon Solenoid . . . . .	17
26	2.2.1 CMS coordinate system . . . . .	18
27	2.2.2 Towards the heart of CMS . . . . .	19
28	2.2.3 Data acquisition . . . . .	28
29	2.2.4 CMS computing model . . . . .	28
30	<b>3 Event generation, simulation and reconstruction</b>	31
31	3.1 Collision event generation . . . . .	31
32	3.1.1 Parton distribution functions and the hard interaction . . . . .	31
33	3.1.2 Parton showering . . . . .	31
34	3.1.3 Hadronisation and decay . . . . .	31
35	3.1.4 Underlying event . . . . .	31
36	3.1.5 Event reconstruction and identification . . . . .	31
37	3.2 Detector simulation . . . . .	31
38	3.3 Physics object reconstruction and identification . . . . .	31
39	3.3.1 The particle flow event reconstruction method . . . . .	31
40	3.3.2 Identification of particles . . . . .	31
41	3.3.3 Calibrations and corrections . . . . .	31

42	<b>4 The search for FCNC involving a top quark and a Z boson</b>	33
43	4.1 Model assumptions . . . . .	33
44	4.2 Data and simulation . . . . .	33
45	4.2.1 Standard Model Background simulation . . . . .	33
46	4.2.2 FCNC signal simulation . . . . .	33
47	4.2.3 Trigger requirements . . . . .	33
48	4.3 Baseline event selection . . . . .	33
49	4.4 Data driven background estimation . . . . .	33
50	4.5 Regions and channels . . . . .	33
51	4.6 Construction of template distributions . . . . .	33
52	4.7 Systematic uncertainties . . . . .	33
53	4.8 Limit setting procedure . . . . .	33
54	4.9 Result and discussion . . . . .	33
55	<b>5 Conclusion and outlook</b>	35
56	<b>Bibliography</b>	37

# 1

57

## Theoretical basis

58 The Standard Model (SM) [1] is a name given in 1970s to a theory describing the fundamental  
59 particles and their interactions. This quantum field theory describes the particles and their  
60 interactions as fields and has successfully incorporated three of the four fundamental forces in  
61 the universe. In [Section 1.1](#), the particle content of the SM is summarised, while [Section 1.2](#)  
62 describes the SM Lagrangian and its symmetries. In [Section 1.3](#), the flavour content of the SM  
63 is highlighted. The successful theory of the SM has some shortcomings which are discussed  
64 in [Section 1.4](#) and lead to searches for a more general theory. One of such a search is using  
65 effective field theory (EFT). In [Section 1.5](#) an EFT model focussing on flavour changing neutral  
66 currents (FCNC) involving a top quark is presented. Its current experimental constraints are  
67 given in [Section 1.6](#).

### 68 1.1 Elementary particles and forces

69 The interactions in nature can be described by four forces, the strong force, the electromagnetic  
70 (EM) force, the weak force and the gravitational force, that are mediated by particles with  
71 an integer spin, bosons. The strong interaction is mediated by eight gluons  $g$ , while the  
72 electromagnetic force is mediated by photons  $\gamma$ , and the weak force by  $Z$  and  $W^\pm$  bosons. In  
73 [Table 1.1](#), the forces and their characteristics are shown. The gravitational force is the only  
74 force not included in the SM and can be neglected for energies lower than the Planck scale  
( $1.22 \cdot 10^{19}$  GeV).

**Table 1.1:** The four forces of nature and their characteristics.

	Range	Mediator
Strong force	$10^e - 15$ m	8 gluons
Electromagnetic force	$\infty$	photon
Weak force	$10^{-18}$ m	$W^\pm$ , Z bosons
Gravitational force	$\infty$	unknown

75

76 The fermions are the particles that make up the visible matter in the universe. They carry half  
77 integer spin and can be subdivided into leptons and quarks, where leptons don't interact strongly.

78 Each fermion has a corresponding anti-fermion which has the same mass and is oppositely  
 79 charged. The electron  $e^-$  is the first elementary particle discovered [2] and belongs to the first  
 80 generation of leptons together with electron neutrino  $\nu_e$ . The second generation is made up  
 81 of the muon  $\mu^-$  and the muon neutrino  $\nu_\mu$ , whereas the third generation consists of the tau  
 82  $\tau$  and the tau neutrino  $\nu_\tau$ . The neutrino's are neutral particles, while the other leptons have  
 83 charge  $\pm q_e$  where  $q_e$  represents the elementary charge of  $1.602 \cdot 10^{-19}$  C. The masses of the  
 84 charged leptons differ by four orders of magnitude between the first and third generations. In  
 85 the SM the neutrino's are assumed to be massless, while it is experimentally established that  
 86 neutrino do have a tiny non-zero mass. In Table 1.2, the leptons and their properties in the SM  
 are summarised.

**Table 1.2:** The properties of the leptons in the three generations of the SM [3], where  $q_e$  represents the elementary charge.

Generation	Particle	Mass	Charge
First	$e^-$	0.511 MeV	$-q_e$
	$\nu_e$	$\approx 0$	0
Second	$\mu^-$	106 MeV	$-q_e$
	$\nu_\mu$	$\approx 0$	0
Third	$\tau$	1 777 MeV	$-q_e$
	$\nu_\tau$	$\approx 0$	0

87

88 The quarks can also be divided into three generations. Unlike the leptons, they carry colour  
 89 charge and can interact via the strong interaction. The top quark, discovered in 1995 at the  
 90 Tevatron [4, 5] is the heaviest SM particle with a mass close to  $173.1 \pm 0.6$  GeV<sup>1</sup> [3]. The  
 quarks and their properties are summarized in Table 1.3.

**Table 1.3:** The properties of the quarks in the three generations of the SM [3], where  $q_e$  represents the elementary charge.

Generation	Particle	Mass	Charge
First	up u	$2.2^{+0.6}_{-0.4}$ MeV	$\frac{2}{3} q_e$
	down d	$4.7^{+0.5}_{-0.4}$ MeV	$\frac{-1}{3} q_e$
Second	charm c	$1.28 \pm 0.03$ GeV	$\frac{2}{3} q_e$
	strange s	$96^{+8}_{-4}$ MeV	$\frac{-1}{3} q_e$
Third	top t	$173.1 \pm 0.6$ GeV	$\frac{2}{3} q_e$
	bottom b	$4.18^{+0.04}_{-0.03}$ GeV	$\frac{-1}{3} q_e$

91

92 The scalar boson, commonly known as the Higgs boson, is the last piece of the SM and is  
 93 discovered in 2012 [6, 7]. It is responsible for the masses of the  $W^\pm$  and Z boson, and that of  
 94 the fermions.

---

<sup>1</sup>In this thesis all masses and energies are expressed in natural units, where the speed of light and  $\hbar$  are taken to be equal to one.

## 95 1.2 Standard Model Lagrangian

96 The SM is a quantum field theory and thus describes the dynamics and kinematics of particles  
 97 and forces by a Lagrangian  $\mathcal{L}$ . The theory is based on the  $SU_C(3) \times SU_L(2) \times U_Y(1)$  gauge  
 98 symmetry, where  $SU_L(2) \times U_Y(1)$  describes the electroweak interaction and  $SU_C(3)$  the strong  
 99 coupling. The indices refer to colour C, the left chiral nature of the  $SU_L(2)$  coupling L, and the  
 100 weak hypercharge Y. Its Lagrangian is constructed such that contains symmetries representing  
 101 physics conservation laws such as conservation of energy, momentum and angular momentum.  
 102 By imposing gauge invariance the symmetries under local group transformations are sustained.

The  $U_Y(1)$  group has one generator Y with an associated gauge field  $B_\mu$ . The three gauge fields  $W_\mu^1$ ,  $W_\mu^2$ , and  $W_\mu^3$ , are associated to  $SU_L(2)$  with three generators that can be written as half of the Pauli matrices:

$$T_1 = \frac{1}{2} \begin{pmatrix} 0 & 1 \\ 1 & 0 \end{pmatrix}, \quad T_2 = \frac{1}{2} \begin{pmatrix} 0 & -i \\ i & 0 \end{pmatrix}, \quad T_3 = \frac{1}{2} \begin{pmatrix} 1 & 0 \\ 0 & -1 \end{pmatrix}. \quad (1.1)$$

The generators  $T^a$  satisfy the Lie algebra:

$$[T^a, T^b] = i\epsilon^{abc} T_c \text{ and } [T^a, Y] = 0, \quad (1.2)$$

103 where  $\epsilon^{abc}$  is an antisymmetric tensor. The gauge fields of  $SU_L(2)$  only couple to left-handed  
 104 fermions as required by the observed parity violating nature of the weak force. The  $SU_C(3)$   
 105 group represents quantum chromodynamics (QCD). It has eight generators corresponding to  
 106 eight gluon fields  $G_\mu^{1\dots 8}$ . Unlike  $SU_L(2) \times U_Y(1)$ ,  $SU_C(3)$  is not chiral.

Under  $SU_C(3)$  quarks are colour triplets while leptons are colour singlets. This implies that the quarks carry a colour index ranging between one and three, whereas leptons do not take part in strong interactions. Based on the chirality, the quarks and leptons are organized in doublets or singlets. Each generation  $i$  of fermions consists of these left-handed doublets and right-handed singlets:

$$l_L = \begin{pmatrix} e^-_L \\ \nu_L \end{pmatrix}, \quad e^-_R, \quad q_L = \begin{pmatrix} u_L \\ d_L \end{pmatrix}, \quad u_R, \quad \text{and } d_R \quad (1.3)$$

The SM Lagrangian can be decomposed as a sum of four terms

$$\mathcal{L}_{SM} = \mathcal{L}_{gauge} + \mathcal{L}_f + \mathcal{L}_{Yuk} + \mathcal{L}_\phi, \quad (1.4)$$

107 that are related to the gauge, fermion, Yukawa and scalar sectors. The gauge Lagrangian  
 108 regroups the gauge fields of all three symmetry groups, and the fermionic part consists of kinetic  
 109 energy terms for quarks and leptons. The interaction between fermions and the scalar doublet  
 110  $\phi$  gives rise to fermion masses and is described by the Yukawa Lagrangian. The scalar part of  
 111 the Lagrangian is composed of a kinematic and potential component related to the scalar boson.

For the electroweak theory, two coupling constants are introduced, namely  $g'$  for  $U_Y(1)$  and  $g$  for  $SU_L(2)$ . The physically observable gauge bosons of this theory are the photon field  $A_\mu$ , the

**NOTE:**  
should I explain gauge invariance or is a reference enough?

$Z_\mu^0$ , and  $W_\mu^\pm$ . These are a superposition of the four gauge fields of  $SU_L(2) \times U_Y(1)$ :

$$A_\mu = \sin\theta_W W_\mu^1 + \cos\theta_W B_\mu, Z_\mu^0 = \cos\theta_W W_\mu^3 - \sin\theta_W B_\mu, \text{ and } W_\mu^\pm = \sqrt{\frac{1}{2}} (W_\mu^1 \mp W_\mu^2), \quad (1.5)$$

where  $\theta_W$  represents the weak mixing angle defined as  $\tan\theta_W = \frac{g'}{g}$ .

The coupling constant representing the strength of the QCD interactions is denoted as  $g_s$ . In QCD there is asymptotic freedom whereby the strong coupling constant becomes weaker as the energy with which the interaction between strongly interacting particles is probed increases, and stronger as the distance between the particles increases. A consequence of this is known as colour confinement. The quarks and gluons can not exist on their own and are not observed individually. They are bound in colour neutral states called hadrons, this process is known as hadronisation.

## Electroweak symmetry breaking

In  $\mathcal{L}_{\text{gauge}}$  and  $\mathcal{L}_f$  are no mass terms for fermions present because only singlets under  $SU_C(3) \times SU_L(2) \times U_Y(1)$  can acquire a mass with an interaction of the type  $m^2 \phi^\dagger \phi$  without breaking the gauge invariance. In order to accommodate mass terms for fermions and gauge fields, electroweak symmetry breaking, leading to  $\mathcal{L}_\phi$  is introduced.

The scalar doublet is introduced in the SM as

$$\phi = \frac{1}{\sqrt{2}} \begin{pmatrix} \varphi_1 + i\varphi_2 \\ \varphi_3 + i\varphi_4 \end{pmatrix}. \quad (1.6)$$

**NOTE:**  
check if I  
need to add  
constants  
here

Its field potential is of the form

$$V(\phi) = \mu^2 \phi^\dagger \phi + \lambda (\phi^\dagger \phi)^2, \quad (1.7)$$

with  $\mu^2 < 0$  and  $\lambda$  a positive integer. This choice of parameters gives the potential a "Mexican hat" shape. It has an infinite set of minima (ground states) and by expanding the field around an arbitrary choice of ground state, the electroweak symmetry is broken (EW):

$$\phi = \begin{pmatrix} 0 \\ \frac{v}{\sqrt{2}} \end{pmatrix} + \hat{\phi}, \quad (1.8)$$

where  $v$  is the vacuum expectation value (vev), measured to be around 245 GeV and corresponds to  $\sqrt{\frac{-\mu}{\lambda}}$ . The scalar doublet's four degrees of freedom is reduced to three degrees of freedom that couple to the gauge fields and mix with the  $W^+$ ,  $W^-$  and  $Z$  bosons. The remaining fourth degree of freedom has given rise to a physically observable particle, called the Brout-Englert-Higgs (BEH) boson. This spontaneous symmetry breaking leaves the gauge invariance intact and gives masses to the  $W^\pm$  and  $Z$  bosons as:

$$m_W = \frac{1}{2} v |g| \quad \text{and} \quad m_Z = \frac{1}{2} v \sqrt{g'^2 + g^2}. \quad (1.9)$$

The Brout-Englert-Higgs field couples universally to fermions with a strength proportional to their masses, and to gauge bosons with a strength proportional to the square of their masses.

### <sup>127</sup> 1.3 Flavour changing currents in the SM

Flavour changing charged currents are introduced in 1963 by Nicola Cabibbo . Via interaction with a W boson the flavour of the quarks is changed. At the time of the postulation, only up, down and strange quarks were known and the charged weak current was described as a coupling between the up quark and d<sub>weak</sub>, where d<sub>weak</sub> is a linear combination of the down and strange quarks, d<sub>weak</sub> = cosθ<sub>c</sub>d + sinθ<sub>c</sub>s. This linear combination is a direct consequence of the chosen rotation

$$\begin{pmatrix} d_{\text{weak}} \\ s_{\text{weak}} \end{pmatrix} = \begin{pmatrix} \cos\theta_c & \sin\theta_c \\ -\sin\theta_c & \cos\theta_c \end{pmatrix} \begin{pmatrix} d \\ s \end{pmatrix} = \mathcal{R} \begin{pmatrix} d \\ s \end{pmatrix}, \quad (1.10)$$

where the rotation angle θ<sub>c</sub> is known as the Cabibbo angle. This provides a definition for the charged weak current between u and d quarks,

$$J_\mu = \bar{u} \gamma_\mu (1 + \gamma_5) d_{\text{weak}}. \quad (1.11)$$

A consequence of Cabibbo's approach is that the s<sub>weak</sub> is left uncoupled, leading to Glashow, Iliopoulos and Maiani (GIM) to require the existence of a fourth quark with charge  $\frac{2}{3}$ . This quark, known as the charm quark, couples to s<sub>weak</sub> and a new definition of the charged weak current is modified to

$$J_\mu = (u \ c) \gamma_\mu (1 + \gamma_5) \mathcal{R} \begin{pmatrix} d \\ s \end{pmatrix} = \bar{U} \gamma_\mu (1 + \gamma_5) \mathcal{R} D. \quad (1.12)$$

The neutral weak current is defined as

$$J_3 = \bar{U} \gamma_\mu (1 + \gamma_5) [\mathcal{R}, \mathcal{R}^\dagger] D, \quad (1.13)$$

<sup>128</sup> and is diagonal in flavour space. This has as consequence that no flavour changing neutral currents occur at tree-level Feynmann diagrams<sup>2</sup> .

Kobayashi and Maskawa generalised the Cabibbo rotation matrix to accommodate for a third generation of quarks. The result is a  $3 \times 3$  unitary matrix known as the CKM matrix, responsible for the mixing of weak interaction states of down-type quarks:

$$\begin{pmatrix} d_{\text{weak}} \\ s_{\text{weak}} \\ b_{\text{weak}} \end{pmatrix} = \begin{pmatrix} V_{ud} & V_{us} & V_{ub} \\ V_{cd} & V_{cs} & V_{cb} \\ V_{td} & V_{ts} & V_{tb} \end{pmatrix} \begin{pmatrix} d \\ s \\ b \end{pmatrix} = \mathcal{V}_{\text{CKM}} \begin{pmatrix} d \\ s \\ b \end{pmatrix}. \quad (1.14)$$

The unitarity of the matrix ( $\mathcal{V}_{\text{CKM}}^\dagger \mathcal{V}_{\text{CKM}} = \mathbb{1}$ ). A general  $3 \times 3$  unitary matrix depends on three real angles and six phases. For the CKM matrix, the freedom to redefine the phases of the quark eigenstates can remove fives of the phases, leaving a single physical phase known as the Kobayashi-Maskawa phase. This phase is responsible for the charge parity violation in the

<sup>2</sup>Feynmann diagrams are physical representation of interaction between particles. They are based on Feynmann rules [1].

**NOTE:** Add source

**NOTE:** Add source

**NOTE:** should I explain feynmann diagrams?

**NOTE:** Add source

SM [8]. Each element  $V_{ij}$  of  $\mathcal{V}_{CKM}$  represents the transition probability of a quark  $i$  going to a quark  $j$ , and is experimentally determined to be [3]

$$\mathcal{V}_{CKM} = \begin{pmatrix} 0.97425 \pm 0.00022 & 0.2253 \pm 0.0008 & (4.13 \pm 0.49)10^{-3} \\ 0.225 \pm 0.008 & 0.986 \pm 0.016 & (41.1 \pm 1.3)10^{-3} \\ (8.4 \pm 0.6)10^{-3} & (40.0 \pm 2.7)10^{-3} & 1.021 \pm 0.032 \end{pmatrix}. \quad (1.15)$$

From Equation 1.15 follows that top quarks predominantly decay via charged weak currents to bottom quarks, with a probability consistently with unity. In the SM, FCNC can only occur via higher loop Feynmann diagrams which are highly suppressed. The expected transition probabilities for a top quark decaying via a FCNC interaction in the SM are given in Table 1.4, where it is clear that the FCNC sector of the SM is still beyond the reach of the sensitivity of current experiments.

**Table 1.4:** The predicted branching ratios  $\mathcal{B}$  for FCNC interactions involving the top quark in the SM [9]

Process	$\mathcal{B}$ in the SM	Process	$\mathcal{B}$ in the SM
$t \rightarrow uZ$	$8 \cdot 10^{-17}$	$t \rightarrow cZ$	$1 \cdot 10^{-14}$
$t \rightarrow u\gamma$	$4 \cdot 10^{-16}$	$t \rightarrow c\gamma$	$5 \cdot 10^{-14}$
$t \rightarrow ug$	$4 \cdot 10^{-14}$	$t \rightarrow cg$	$5 \cdot 10^{-12}$
$t \rightarrow uH$	$2 \cdot 10^{-17}$	$t \rightarrow cH$	$3 \cdot 10^{-15}$

135

## 1.4 Motivations for new physics

Many high energy experiments confirm the success of the SM. In particular the scalar boson, the cornerstone of the SM, has consecrated the theory. Unfortunately there are also strong indications that the SM ought to be a lower energy expression of a more global theory. The existence of physics beyond the SM(BSM) [10] is strongly motivated. These motivations are based on direct evidence from observation such as the existence of neutrino masses, the existence of dark matter and dark energy, or the matter-antimatter asymmetry, and also from theoretical problems such as the hierarchy problem, the coupling unification or the large numbers of free parameters in the SM.

In the SM, the neutrino is assumed to be massless, whilst experiments with solar, atmospheric, reactor and accelerator neutrinos have established that neutrinos can oscillate and change flavour during flight. These oscillations are only possible when neutrino's have masses. The flavour neutrinos ( $\nu_e$ ,  $\nu_\mu$ ,  $\nu_\tau$ ) are then linear expressions of the fields of at least three mass eigenstate neutrinos  $\nu_1$ ,  $\nu_2$ , and  $\nu_3$ .

The ordinary or baryonic matter described by the SM describes only 5% of the mass (energy) content of the universe. Astrophysical evidence indicated that dark matter is contributing to approximately 27%, and dark energy to 68% of the content of the universe. From the measurements of the temperature and polarizations anisotropies of the cosmic microwave background by the Planck experiment, the density of cold non baryonic matter is determined. Dark energy is responsible for the acceleration with the expansion of the universe.

**NOTE:** Reread and elaborate

139

**NOTE:** Add source

148

**NOTE:** Add source

155

At the big bang matter and antimatter is assumed to be produced in equal quantities. However, it is clear that we are surrounded by matter. So where did all the antimatter go? In 1967, Sakharov identified three mechanisms that are necessary to obtain a global matter antimatter asymmetry [11]. These mechanisms are baryon and lepton number violation, at a given moment in time there was a thermal imbalance for the interactions in the universe, and there is charge C and charge parity CP violation<sup>3</sup>. The large numbers of free parameters in the SM are taken as nine fermion masses, three CKM mixing angles and one CP violating phase, one EM coupling constant  $g'$ , one weak coupling constant  $g$ , one strong coupling constant  $g_s$ , one QCD vacuum angle, one vacuum expectation value, and one mass of the scalar boson. This large number of free parameters lead to the expectation of a more elegant, general theory beyond the SM.

The hierarchy problem is related to the huge difference in energy between the weak scale and the Planck scale. The vev of the Brout-Englert-Higgs field determines the weak scale that is approximately 246 GeV. The radiative corrections to the scalar boson squared mass  $m_H^2$ , coming from its self couplings and couplings to fermions and gauge bosons, are quadratically proportional to the ultraviolet momentum cut-off  $\Lambda_{UV}$ . This cut-off is at least equal to the energy to which the SM is valid without the need of new physics. The SM is valid up to the Planck mass making the correction to  $m_H^2$  about thirty orders of magnitude larger than  $m_H^2$ . This implies that an extraordinary cancellation of terms should happen. This is also known as the naturalness problem of the H boson mass .

**NOTE:** Add source

**NOTE:** Add source

The correction to the squared mass of the scalar boson coming from a fermion  $f$ , coupling to the scalar field  $\phi$  with a coupling  $\lambda_f$  is given by

$$\Delta m_H^2 = -\frac{|\lambda_f|^2}{8\pi^2} \Lambda_{UV}^2, \quad (1.16)$$

while the correction to the mass from a scalar particle  $S$  with a mass  $m_S$ , coupling to the scalar field with a Lagrangian term  $-\lambda_{S|f} |\phi|^2 |S|^2$  is

$$\Delta m_H^2 = -\frac{|\lambda_S|^2}{16\pi^2} \left( \Lambda_{UV}^2 - 2m_S^2 \ln \left( \frac{\Lambda_{UV}}{m_S} \right) + \dots \right). \quad (1.17)$$

As one can see the correction term to  $m_H^2$  is much larger than  $m_H^2$  itself. By introducing BSM physic models that introduce new scalar particles at TeV scale that couple to the scalar boson can cancels the  $\Lambda_{UV}^2$  divergence and avoid this fine-tuning.

**NOTE:** Add source

Also the large mass differences between the fermions related to the Yukawa couplings can go up to six order of magnitude in the case of the electron and the top quark and constitute the fermion mass hierarchy problem .

**NOTE:** Add source

The choice of the  $SU_C(3) \times SU_L(2) \times U_Y(1)$  symmetry group itself as well as the seperate treatment of the three forces included in the SM raises concern. The intensity of the forces

<sup>3</sup>The rate of a process  $i \rightarrow f$  can be different from the CP-conjugate process:  $\tilde{i} \rightarrow \tilde{f}$ . The SM includes sources of CP-violation through the residual phase of the CKM matrix. However, these could not account for the magnitude of the asymmetry observed.

183 show a large disparity around the electroweak scale, but have comparable strengths at higher  
 184 energies. The electromagnetic and weak forces are unified in a electroweak interaction, but the  
 185 strong coupling constant does not encounter the other coupling constants at high energies. In  
 186 order to reach a grand unification, the running of couplings can be modified by the addition of  
 new particles in BSM models .

**NOTE:** Add 7  
source

## 188 1.5 An effective approach beyond the SM: FCNC involving a top 189 quark

190 The closeness of the top mass to the electroweak scale led physicist to believe that it is a sensitive  
 191 probe for new physics. Its property study is therefore an important topic of the experimental  
 192 program at the LHC. Several extensions of the SM enhance the FCNC branching ratios and can  
 193 be probed at the LHC [9], from which some of them are shown in [Table 1.5](#). Previous searches  
 194 have been performed at the Fermilab Tevatron by the CDF [12] and D0 [13] collaborations,  
 and at the LHC by the ATLAS [14, 15] and CMS [16–18] collaborations.

**NOTE:**  
check  
with refer-  
ences from  
TOP2017

**Table 1.5:** The predicted branching ratios  $\mathcal{B}$  for FCNC interactions involving the top quark in some BSM models [9]: quark singlet (QS), generic two Higgs doublet model (2HDM) and the minimal super symmetric extensions to the SM (MSSM);

Process	QS	2HDM	MSSM	Process	QS	2HDM	MSSM
$t \rightarrow uZ$	$\leq 1.1 \cdot 10^{-4}$	—	$\leq 2 \cdot 10^{-6}$	$t \rightarrow cZ$	$\leq 1.1 \cdot 10^{-4}$	$\leq 10^{-7}$	$\leq 2 \cdot 10^{-6}$
$t \rightarrow u\gamma$	$\leq 7.5 \cdot 10^{-9}$	—	$\leq 2 \cdot 10^{-6}$	$t \rightarrow c\gamma$	$\leq 7.5 \cdot 10^{-9}$	$\leq 10^{-6}$	$\leq 2 \cdot 10^{-6}$
$t \rightarrow ug$	$\leq 1.5 \cdot 10^{-7}$	—	$\leq 8 \cdot 10^{-5}$	$t \rightarrow cg$	$\leq 1.5 \cdot 10^{-7}$	$\leq 10^{-4}$	$\leq 8 \cdot 10^{-5}$
$t \rightarrow uH$	$\leq 4.1 \cdot 10^{-5}$	$\leq 5.5 \cdot 10^{-6}$	$\leq 10^{-5}$	$t \rightarrow cH$	$\leq 4.1 \cdot 10^{-5}$	$\leq 10^{-3}$	$\leq 10^{-5}$

195

196 The impact of BSM models can written in a model independent way by means of an effective  
 197 field theory valid up to an energy scale  $\Lambda$ . The leading effects are parametrized by a set of  
 198 fully gauge symmetric dimension-6 operators that are added to the SM Lagrangian and can be  
 199 reduced to a minimal set of operators as discussed in [19, 20]. The full Lagrangian, neglecting  
 200 neutrino physics, in the fully gauge symmetric case is given by

$$\mathcal{L}_{\text{SM+EFT}} = \mathcal{L}_{\text{SM}} + \sum_i \frac{\bar{c}_i}{\Lambda^2} \mathcal{O}_i + \mathcal{O}\left(\frac{1}{\Lambda^3}\right), \quad (1.18)$$

where the Wilson coefficients  $\bar{c}_i$  depend on the considered theory and on the way that new physics couples to the SM particles. Considering that  $\Lambda$  is large, contributions suppressed by powers of  $\Lambda$  greater than two are neglected. Moreover, all four fermion operators are omitted for the rest of this thesis. After electroweak symmetry breaking the operators induce [9, 21] both corrections to the SM couplings and new interactions at tree level such as FCNC interactions.

The FCNC interactions of the top quark that are not present in the SM are given by

$$\mathcal{L}_{\text{EFT}}^t = \frac{\sqrt{2}}{2} \sum_{q=u,c} \left[ g' \frac{\kappa_{t\gamma q}}{\Lambda} A_{\mu\nu} \bar{t} \sigma^{\mu\nu} (f_{\gamma q}^L P_L + f_{\gamma q}^R P_R) q \right. \quad (1.19)$$

$$+ \frac{g}{2\cos\theta_W} \frac{\kappa_{tZq}}{\Lambda} Z_{\mu\nu} \bar{t} \sigma^{\mu\nu} (f_{Zq}^L P_L + f_{Zq}^R P_R) q \quad (1.20)$$

$$+ \frac{\sqrt{2}}{4\cos\theta_W} \zeta_{tZq} \bar{t} \gamma^\mu (\tilde{f}_q^L P_L + \tilde{f}_q^R P_R) q Z_\mu \quad (1.21)$$

$$+ g_S \frac{\kappa_{gqt}}{\Lambda} Z_{\mu\nu} \bar{t} \sigma^{\mu\nu} (f_{gq}^L P_L + f_{gq}^R P_R) q G_{\mu\nu}^a \quad (1.22)$$

$$+ \eta_{Hqt} \bar{t} (\hat{f}_q^L P_L + \hat{f}_q^R P_R) q H + \text{h.c.} \Big], \quad (1.23)$$

where the the value of the FCNC couplings at scale  $\Lambda$  are represented by  $\kappa_{tZq}, \kappa_{gqt}, \kappa_{t\gamma q}, \zeta_{tZq}$ , and  $\eta_{Hqt}$ . These are assumed to be real and positive, with the unit of  $\text{GeV}^{-1}$  for  $\kappa_{tXq}/\Lambda$  and no unit for  $\zeta_{xqt}$  and  $\eta_{xqt}$ . In the equation  $\sigma^{\mu\nu}$  equals to  $\frac{i}{2} [\gamma^\mu, \gamma^\nu]$ , and the left- and right-handed chirality projector operators are denoted by  $P_L$  and  $P_R$ . The electromagnetic coupling constant is denoted by  $g'$ , the strong interaction coupling is denoted as  $g_s$ , while the electroweak interaction is parametrised by the coupling constant  $g$  and the electroweak mixing angle  $\theta_W$ . The complex chiral parameters are normalized according to  $|f_{xq}^L|^2 + |f_{xq}^R|^2 = 1$ ,  $|\tilde{f}_q^L|^2 + |\tilde{f}_q^R|^2 = 1$ , and  $|\hat{f}_q^L|^2 + |\hat{f}_q^R|^2 = 1$ . In the expression for  $\mathcal{L}_{\text{EFT}}^t$ , the unitary gauge is adopted on the scalar field is expanded around its vacuum expectation value with  $H$  being the SM scalar boson, and the field strength tensors of the photon  $A_\mu$ , the gluon field  $G_\mu^{1..8}$ , and the Z boson  $Z_\mu^0$  are defined as

$$A_{\mu\nu} = \partial_\mu A_\nu - \partial_\nu A_\mu, Z_{\mu\nu} = \partial_\mu Z_\nu - \partial_\nu Z_\mu, \text{ and } G_{\mu\nu} = \partial_\mu G_\nu^a - \partial_\nu G_\mu^a + g_S f_{bc}^a G_\mu^b G_\nu^c. \quad (1.24)$$

201 Denoting the structure constant of the  $SU_C(3)$  group as  $f_{bc}^a$ . Note that there are two coupling  
 202 constants arising in  $\mathcal{L}_{\text{EFT}}^t$ , which is a residu of electroweak symmetry breaking. The massive Z  
 203 boson will appear in both the  $Z_\mu^0$  field as well as the covariant derivative, leading to an extra  
 204 Z-vertex.

## 205 1.6 Experimental constraints on top-FCNC

Experiments commonly put limits on the branching ratio's which allow an easier interpretation across different EFT models as

$$\mathcal{B}(t \rightarrow qX) = \frac{\delta_{tXq}^2 \Gamma_{t \rightarrow qX}}{\Gamma_t}, \quad (1.25)$$

206 where  $\Gamma_{t \rightarrow qX}$  represents the FCNC decay width<sup>4</sup> for a coupling strength  $\delta_{tXq}^2 = 1$ , and  $\Gamma_t$  the full  
 207 decay width of the top quark. In the SM, supposing a top quark mass of 172.5 GeV, the full  
 208 width becomes  $\Gamma_t^{\text{SM}} = 1.32 \text{ GeV}$  [22].

<sup>4</sup>The decay width of a certain process represents the probability per unit time that a particle will decay. The total decay width, defined as all possible decay widths of a particle, is inversely proportional to its lifetime.

209 Searches for top-FCNC usually adopt a search strategy depending on the experimental setup  
 210 and the FCNC interaction of interest, looking either for FCNC interactions in the production of  
 211 a single top quark or in its decay for top pair interactions. In [Figure 1.1](#), these two cases are  
 212 shown for the tZq vertex.

213

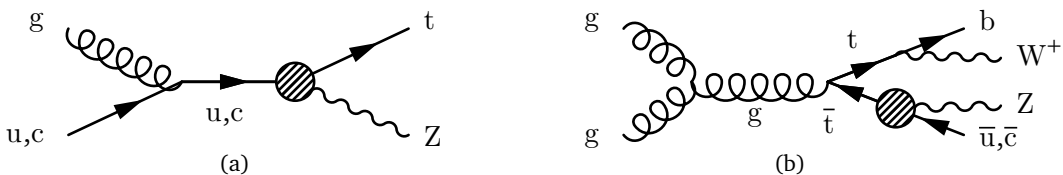


**Figure 1.1:** Feynman diagrams for the tZq FCNC interaction, where the FCNC interaction is indicated with the shaded dot. Left: single top production through an FCNC interaction. Right: top pair production with an FCNC induced decay.

214 The observation of top-FCNC interactions has yet to come and experiments have so far only  
 215 been able to put upper bounds on the branching ratios. An overview of the best current limits  
 216 is given in [Table 1.6](#). In [Figure 1.2](#) a comparison is shown between the current best limits  
 217 set by ATLAS and CMS with respect to several BSM model benchmark predictions. From there  
 218 one can see that FCNC searches involving a Z or H boson are close to excluding or confirming  
 219 several BSM theories.

**Table 1.6:** The four forces of nature and their characteristics.

Process	Search mode	Observed $\mathcal{B}$	Expected $\mathcal{B}$	Reference
---------	-------------	------------------------	------------------------	-----------

219

## 220 1.7 Statistics for a high energy particle physicist

### 221 1.7.1 Boosted decision trees

### 222 1.7.2 Confidence levels

### 223 1.7.3 Combine limit setting tool

**NOTE:** update after TOP2017

218

**NOTE:** update figure after TOP2017

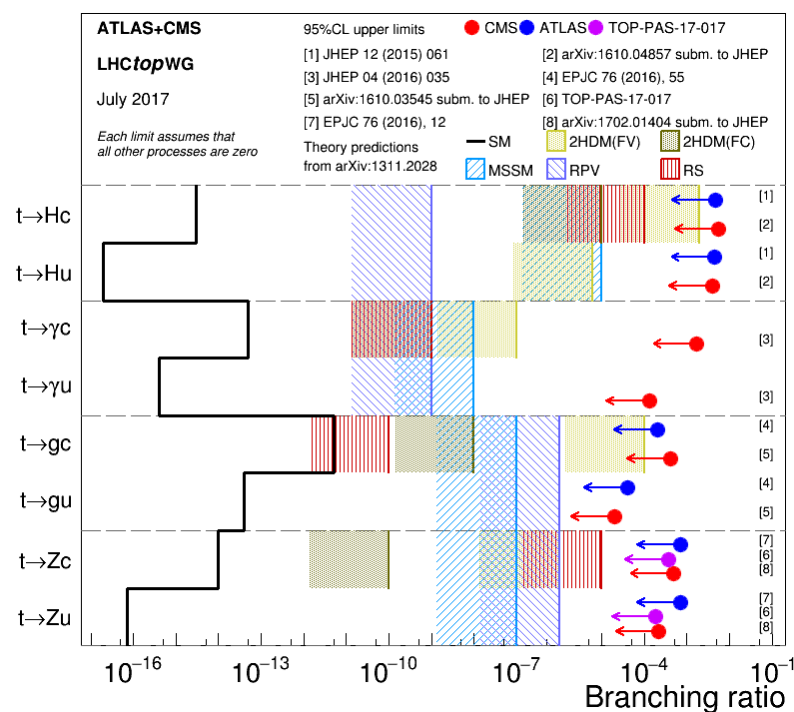


**Figure 1.2:** Current best limits set by CMS and ATLAS for top-FCNC interactions.



# Experimental set-up

# 2

225 The main objective of the Large Hadron Collider (LHC) was the search for the Brout-Englert-  
 226 Higgs boson (or scalar boson). It was known from the Linear Electron Positron(LEP)[23] and  
 227 Tevatron[24] experiments that the scalar boson mass had to be larger than 114 GeV[25, 26],  
 228 and smaller than around 1 TeV due to unitarity and perturbativity constraints [27]. On top of  
 229 this, the search of supersymmetry or dark matter were part of the motivation for building the  
 230 LHC. Since the start of its operation, the LHC is pushing the boundaries of the Standard Model,  
 231 putting the best limits on physics beyond the Standard Model as well as precision measurements  
 232 of the parameters of the Standard Model. One such an accomplishment is the discovery the  
 233 scalar boson in 2012 by the two largest experiments at the LHC [6, 7].

234 In the first part of this chapter, the LHC and the acceleration process for protons to reach  
 235 their design energies is discussed. The second part presents the Compact Muon Solenoid.

## 236 2.1 The Large Hadron Collider

237 The LHC has started its era of cutting edge science on 10 September 2008 [28] after approval by  
 238 the European Organisation of Nuclear Research (CERN) in 1995 [29]. Installed in the previous  
 239 Large Electron Positron collider (LEP) tunnels, the LHC consists of a 26.7 km ring, that is  
 240 installed between 45 and 170 m under the French-Swiss border between Cessy (France) and  
 241 Meyrin (Switzerland). Built to study rare physics phenomena at high energies, the LHC has the  
 242 possibility to accelerate two type of particles - protons or ions  $Pb^{45+}$  - and provides collisions  
 243 at four points of interaction or bunch crossings.. At the interaction points, experiments are  
 244 installed in order to study the collisions.

245 As can be seen in [Figure 2.1](#), the LHC is last element in a chain of creation, injection and  
 246 acceleration of protons. Protons are obtained by ionising hydrogen and injected in a linear  
 247 accelerator (LINAC 2), where they obtain an energy of 50 MeV. They continue to the proton  
 248 synchrotron booster (PSB or Booster), where the proton packets are accelerated to 1.4 GeV and  
 249 are split up in twelve. The proton synchrotron (PS) increases their energy to 25 GeV before  
 250 handing the protons to the super proton synchrotron (SPS), where the proton reach an energy  
 251 of 450 GeV. Each accelerator ring increases in radius in order to reduce the energy loss of the  
 252 protons by synchrotron radiation. This energy loss is proportional to the fourth power of the

253 proton energy and inversely proportional to the bending radius. The protons are then injected  
 254 into opposite directions into the LHC, where they are accelerated to 3.5 TeV (in 2010 and  
 255 2011), 4 TeV (in 2012 and 2013) or 6.5 TeV (in 2015 and 2016) [30]. Before the start up of  
 256 the LHC in 2010, the previous energy record was held by the Tevatron collider at Fermilab,  
 257 colliding proton with antiprotons at  $\sqrt{s} = 1.96$  TeV.

258 The beam has a bunch structure obtained by the injection scheme and properties of the dump  
 259 system. These bunches are obtained in the PS with 25 ns spacing for run II. The operation of  
 260 accelerating and transferring to the LHC is repeated 12 times for each counter-rotating beam.  
 261 When completely filled, the LHC nominally contains 2220 bunches in run II, compared to 1380  
 262 in run I (design: 2200). At full intensity, it would have nearly 2800 bunches but this is limited  
 263 due to SPS.

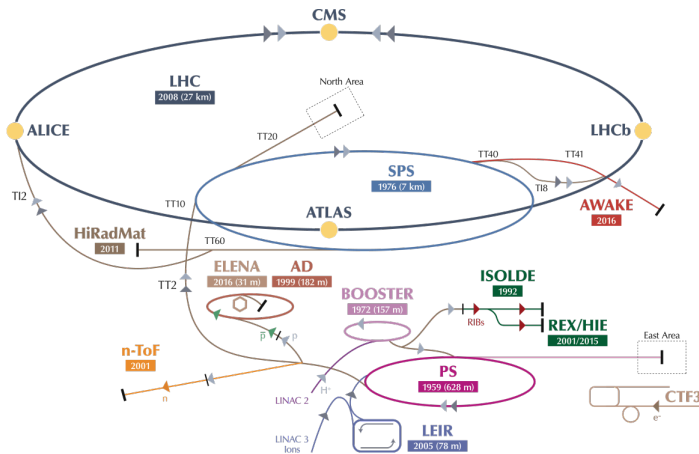


**Figure 2.1:** Schematic representation of the accelerator complex at CERN [31]. The LHC (dark blue) is the last element in chain of accelerators. Protons are successively accelerated by LINAC 2, the Booster, the Proton Synchrotron (PS) and the Super Proton Synchrotron (SPS) before entering the LHC.

264 The LHC is home to seven experiments that are placed on an interaction point:

- 265 • A Toroidal LHC ApparatuS (ATLAS [32]) and the Compact Muon Solenoid (CMS [33])  
 266 experiments are the two general purpose detectors at the LHC. They both have a hermetic,  
 267 cylindrical structure and were designed to search for new physics phenomena as well as  
 268 precision measurements of the Standard Model. The existence of two distinct experiments  
 269 allows cross-confirmation for any discovery.
- 270 • A Large Ion Collider Experiment (ALICE [34]) and the LHC Beauty (LHCb [35]) experiments  
 271 are focusing on specific phenomena. ALICE studies strongly interacting matter  
 272 at extreme energy densities where quark-gluon plasma forms from heavy ions (Pb-Pb or  
 273 p-Pb). LHCb searches for differences between matter and anti matter by means of the b  
 274 quark, while focussing on CP symmetry violation.
- 275 • The forward LHC (LHCf [36]) and the TOTal cross section, Elastic scattering and diffraction  
 276 dissociation Measurement (TOTEM [37]) experiments are two smaller experiments that

277 focus on interactions where protons or heavy ions only meet while head on collisions take  
 278 place. LHCf consists of two parts placed before and after ATLAS and studies particles  
 279 created at very small angles. TOTEM is placed in the same cavern as CMS and performs  
 280 precise measurements of the LHC luminosity.

- 281 • The Monopoles and Exotics Detector At the LHC (MoEDAL [38]) experiment is situated  
 282 near LHCb and tries to find magnetic monopoles.

283 **2.1.1 LHC design and operation**

The most important quantity at the LHC is the luminosity[39]. This is a measurement of the number of collisions that can be produced in a detector per  $\text{m}^2$  and per second. The LHC collisions create a number of events per second given by

$$N_{\text{event}} = L\sigma_{\text{event}}, \quad (2.1)$$

where  $\sigma_{\text{event}}$  is the cross section of the event of interest and  $L$  the machine luminosity. This luminosity depends only on the beam parameters and is for a Gaussian beam expressed as

$$L = \frac{1}{4\pi} \textcolor{blue}{N_b} n_b f_{\text{rev}} \frac{\textcolor{red}{N_b}}{\epsilon_n} \left( 1 + \left( \frac{\theta_c \sigma_z}{2\sigma^*} \right)^2 \right)^{-\frac{1}{2}} \frac{\gamma_r}{\beta^*}. \quad (2.2)$$

284 The number of particles per bunch is expressed by  $N_b$ , while  $n_b$  is the number of bunches  
 285 per beam,  $f_{\text{rev}}$  the revolution frequency,  $\gamma_r$  the relativistic gamma factor,  $\epsilon_n$  the normalized  
 286 transverse beam emittance - a quality for the confinement of the beam ,  $\beta^*$  the beta function at  
 287 the collision point - a measurement for the width of the beam,  $\theta_c$  the angle between the two  
 288 beams at the interaction point,  $\sigma_z$  the mean lengths of one packet, and  $\sigma^*$  the mean height of  
 289 one packet. In Equation 2.2), the blue part represents the stream of particles, the red represents  
 290 the brilliance; and the green part represents the geometric reduction factor due to the crossing  
 291 angle at the interaction point. Hence, in order to enhance the chances for exploration of rare  
 292 events and thus enhancing the number of collisions. High beam energies as well as high beam  
 293 intensities are required.

294 The peak design luminosity for the LHC in 2016 was  $10^{34} \text{ 1}/(\text{m}^2 \text{ s})$ , which leads to about 1  
 295 billion proton interactions per second. In 2016, the LHC was around 10% above this design  
 296 luminosity[40]. This luminosity is not a constant in time. It diminishes due to collisions between  
 297 the beams, and the interaction of the protons and the particle gas that is trapped in the centre  
 298 of the vacuum tubes due to the magnetic field. The intern diffusion of the beam degrades the  
 299 emittance and therefore also the luminosity. For this reason, the mean lifetime of a beam inside  
 300 the LHC is around 15 h. The integrated luminosity - the luminosity provided for a certain time  
 301 range - recorded by CMS and ATLAS over the year 2016 is given in Figure 2.1.1. In Run II, the  
 302 peak luminosity is  $13\text{-}17 \cdot 10^{33} \text{ 1}/(\text{cm}^2 \text{ s})$  compared to  $7.7 \cdot 10^{33} \text{ 1}/(\text{cm}^2 \text{ s})$  in Run I.

303 Inside the LHC ring [41], the protons are accelerated by the means of radio frequency cavities,  
 304 while 1232 magnets of approximately 15 m long, weighing 35 t ensure the deflection of the  
 305 beams. The cross section view of such a dipole is given in Figure 2.4. The two proton beams  
 306 circulate in opposite direction in separate pipes inside of the magnet. Through the use of a strong

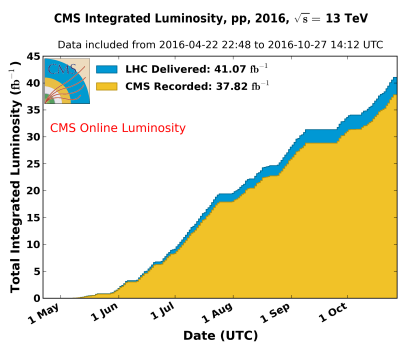


**Figure 2.2:** Cumulative luminosity measured online versus day delivered to (blue), and recorded by CMS (orange) during stable beams and for proton collisions at 13 TeV centre-of-mass energy in 2016. The delivered luminosity accounts for the luminosity delivered from the start of stable beams until the LHC requests CMS to turn off the sensitive detectors to allow a beam dump or beam studies.

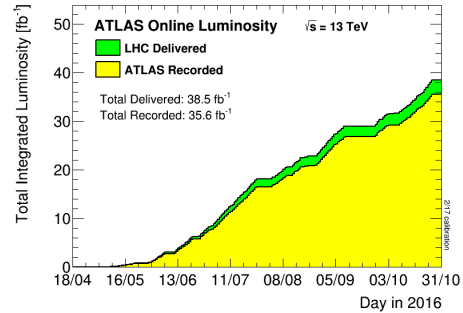


**Figure 2.3:** Total Integrated Luminosity in 2016 Cumulative luminosity versus time delivered to (green) and recorded by ATLAS (yellow) during stable beams for proton collisions in 2016. The delivered luminosity accounts for the luminosity delivered from the start of stable beams until the LHC requests ATLAS to put the detector in a safe standby mode to allow for a beam dump or beam studies. Shown is the luminosity as determined from counting rates measured by the luminosity detectors. )

307 electric current in the coils around the beam pipe, magnetic fields are generated and cause the  
 308 protons to bend in the required orbits. In order to get the coil to become superconducting and  
 309 able to produce - with the aid of an iron return yoke - a strong magnetic field of 8.3 T, the  
 310 magnet structure is surrounded by a vessel. This vessel is filled with liquid Helium making it  
 311 possible to cool down the magnet to 1.9 K. In order to get more focussed and stabilised proton  
 312 beam, other higher-order multipole and corrector magnets are placed along the LHC tunnel.

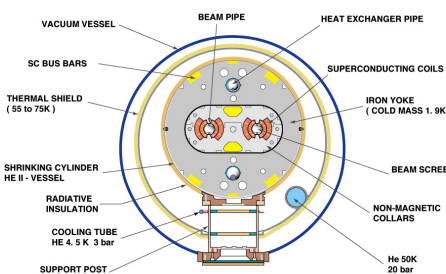


**Figure 2.4:** Schematic representation of the LHC dipole [42]. Two beam pipes where the proton beams circulate around the LHC ring are shown. The superconducting coils generate a magnetic field of 8.3 T that steer the protons in the circular path.

<sup>313</sup> **2.2 The Compact Muon Solenoid**

<sup>314</sup> At one of the collision points of the LHC, the CMS detector[43–45] is placed. Weighing 14 000  
<sup>315</sup> t, This cylindrical detector is about 28.7 m long and 15 m in diameter, weighing around 14 000  
<sup>316</sup> t. It has an onion like structure of several specialised detectors and contains a superconducting  
<sup>317</sup> solenoid with a magnetic field of 3.8 T. The CMS detector is designed in a way that it can  
<sup>318</sup> address the needs of physics coming from the LHC. Living in a hadronic environment, multi-jet  
<sup>319</sup> processes produced by the strong interaction are a main source of background for rare physics  
<sup>320</sup> processes. Therefore, good identification, momentum resolution, and charge determination of  
<sup>321</sup> muon, electrons and photons is one of the main goals of the CMS detector. Further it provides a  
<sup>322</sup> good charged particle momentum resolution and reconstruction efficiency in the inner tracker  
<sup>323</sup> such that for example jets coming from b quarks or tau particles can be identified. Also the  
<sup>324</sup> electromagnetic resolution for an efficient photon and lepton isolation as well as a good hadronic  
<sup>325</sup> calorimeter for the missing transverse energy were kept into account while designing CMS. In  
<sup>326</sup> [Figure 2.5](#), an overview of the CMS detector is given.

<sup>327</sup> The LHC provides many collisions in a short amount of time. In order to discriminate between  
<sup>328</sup> consecutive collisions - known as out of time pile up events - , CMS has to complete the full data  
<sup>329</sup> acquisition for one collision event before the next one happens (around 25 ns in Run II and  
<sup>330</sup> around 50 ns in Run I [46]). Furthermore, since the photons are in packets, around 21 in Run  
<sup>331</sup> I and approximately 40 in Run II inelastic collisions happen every beam crossing . This creates  
<sup>332</sup> a great amount of background processes in the detector called in time pile up events. Due to  
<sup>333</sup> this difficult conditions, the detector has a high granularity which on its turn creates a need for  
<sup>334</sup> huge number of synchronized electronic channels. Furthermore, due to to high flux of particles  
<sup>335</sup> in the regions close to the beam, the electronics have to be able to endure high radiation.

<sup>336</sup> Before the start of taking collision data for 13 TeV operations on 3 June, CMS had a long  
<sup>337</sup> shutdown (LS1)[48]. During this shut down several upgrades were performed. The innermost  
<sup>338</sup> part of detection material in CMS (pixel) is made of three concentric cylindrical layers in  
<sup>339</sup> run I. At the end of 2016 it is upgraded by adding a fourth layer, enhancing the particle  
<sup>340</sup> tracking capabilities of CMS. In order to be able to incorporate this new layer, the section  
<sup>341</sup> of the beryllium beam pipe within CMS was replaced by a narrower one during LS1. For  
<sup>342</sup> this, the pixel was removed and reinserted into CMS. In order to avoid long damage caused  
<sup>343</sup> by the intense particle flux at the heart of CMS, the tracker is been made ready to operate  
<sup>344</sup> at much lower temperature than before. During Run I, a small problem was detected in the  
<sup>345</sup> electromagnetic calorimeter preshower system. For this, the preshower discs were removed,  
<sup>346</sup> repaired and reinstalled successfully inside CMS in 2014. To help the discrimination between  
<sup>347</sup> interesting low momentum muons coming from collisions and muons caused by backgrounds, a  
<sup>348</sup> fourth triggering and measurement station for muons was added in each of the end caps. CMS  
<sup>349</sup> measures the collision rate within the detector and monitors beam related backgrounds. For  
<sup>350</sup> this, several new detectors were installed into CMS during LS1.

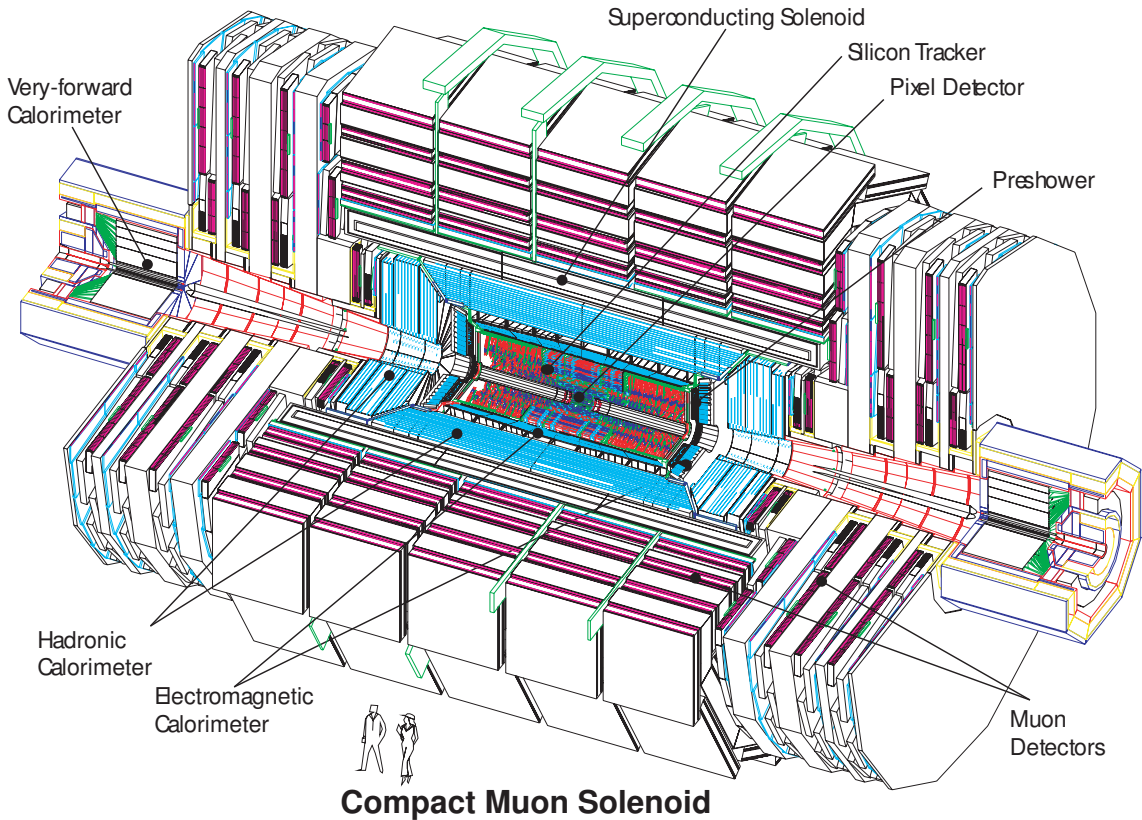


Figure 2.5: Mechanical layout of the CMS detector[47].

### 351 2.2.1 CMS coordinate system

The coordinate system used by CMS can be found in Figure 2.6. The origin of the right handed orthogonal coordinate system is chosen to be the point of collisions. The x-axis points towards the centre of the LHC ring such that the y-axis points towards the sky, and the z-axis lies tangent to the beam axis. Since the experiment has a cylindrical shape, customary coordinates are used to describe the momentum  $\vec{p}$  : the distance  $\rho$ , the azimuthal angle  $\phi \in [-\pi, \pi]$  - the angle between the x-axis and the projection in the transverse plane of  $\vec{p}$  ( $\vec{p}_T$ ) - , the pseudo-rapidity  $\eta$  - expressed by the polar angle  $\theta$  between the direction of  $\vec{p}$  and the beam - :

$$\eta = -\ln\left(\tan\left(\frac{\theta}{2}\right)\right). \quad (2.3)$$

For the energies considered at the LHC, where  $E \gg m$ , the pseudo-rapidity is a good approximation of the rapidity  $y$

$$y = \frac{1}{2} \ln\left(\frac{E + p_z}{E - p_z}\right), \quad (2.4)$$

352 where the difference of rapidities of two particles is invariant under a Lorentz boost in the  
353 z-direction.

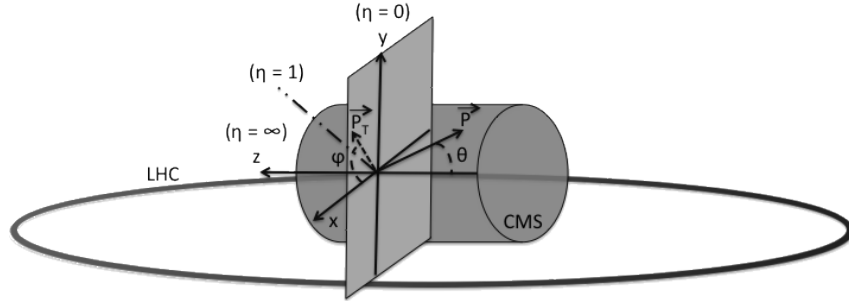


**Figure 2.6:** Representation of the coordinate system used by CMS. The point of origin is put at the collision point. The x-axis points towards the centre of the LHC ring such that the z-axis lies tangent to the beam axis.

### 354 2.2.2 Towards the heart of CMS

355 The CMS detector consists of two parts; a central barrel around the beam pipe ( $|\eta| < 1.4$ ) and  
 356 two plugs to ensure the hermeticity of the detector. In [Figure 2.5](#) and [Figure 2.7](#) the onion like  
 357 structure of the CMS detector is visible. The choice of a solenoid of 12.9 m long and 5.9 m  
 358 diameter gives the advantage of bending the particle trajectories in the transverse plane. The  
 359 hadronic calorimeter, the electromagnetic calorimeter and the tracker are within the solenoid,  
 360 while the muon chambers are placed outside the solenoid.

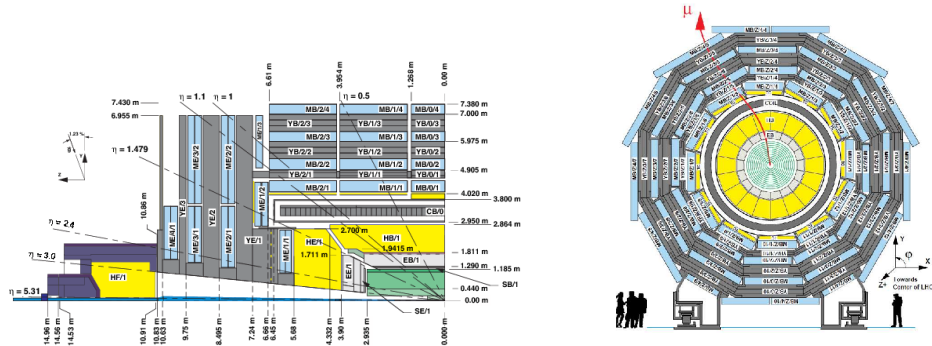


**Figure 2.7:** Schematic view of the CMS detector in the Run I configuration. (LEFT) Longitudinal view of one quarter of the detector. (RIGHT) Transversal view of one quarter of the detector. The muon system barrel elements are denoted as  $MBZ/N/S$ , where  $z = -2 \dots +2$  is the barrel wheel number,  $n = 1 \dots 4$  the station number and  $S = 1 \dots 12$  the sector number. Similarly, the steel return yokes are denoted as  $YBZ/N/S$ . The solenoid is denoted as  $CB0$ , while the hadronic calorimeter is denoted as  $HE$  (end cap)/ $HB$  (barrel)/ $HF$  (forward) and the electromagnetic calorimeter as  $EE$  (end cap)/ $EB$  (barrel). The green part represents the tracking system[49]

#### 361 2.2.2.1 Muon system

362 The outermost part of CMS consists of the muon system. The magnet return yoke is interleaved  
 363 with gaseous detector chambers for muon identification and momentum measurement. The  
 364 barrel contains muon stations arranged in five separate iron wheels, while in the end cap four

365 muon stations are mounted onto three independent iron discs on each side. Each barrel wheel  
 366 has 12 sectors in the azimuthal angle.

367 The muon system is divided into three parts, shown in Figure 2.8[49]. The muon rate and  
 368 neutron induced backgrounds are small and the magnetic field is very low for the barrel, thus  
 369 CMS can use drift tube (DT) chambers. For the end caps however, the muon and background  
 370 flux is much higher and there is a need to use cathode strip chambers (CSC) which are able  
 371 to provide a faster response, higher granularity and have a better resistance against radiation.  
 372 In order to form a redundant trigger system, resistive plate chambers (RPC) are added. This  
 373 makes a total of 250 DT chambers, 540 CSC and 610 RPC. In Figure 2.7 the arrangement is  
 374 shown.

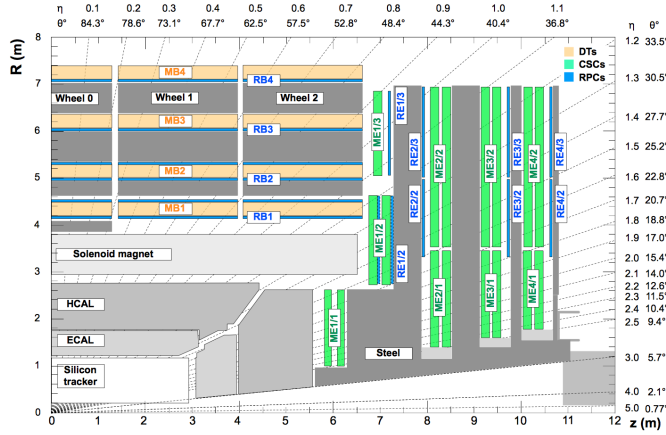


Figure 2.8: Schematic view of one quarter of the CMS muon system in the Run I configuration. [49]

375 Providing a measurement for  $|\eta| < 1.2$ . The DT chambers in the barrel are on average  $2 \times 2.5$  m in size and consist of 12 layers of DT cells - 4 cm wide gas tubes with positively  
 376 charged stretched wire inside - arranged in three groups of four. The  $r\phi$  coordinate is provided  
 377 by the two outside groups, while the middle group measures the  $z$  coordinate. For each  $\phi$   
 378 sector, the DT chamber is mixed with the flux return yoke. For the outer muon station, the DT  
 379 chamber contains only 8 layers of DT cells, providing a muon position in the  $r\phi$  plane. There are  
 380 four CSC stations in each end cap, providing muon measurements for  $0.9 < |\eta| < 2.4$  (Run I  
 381 configuration). These CSC are multi-wired proportional chambers that consist of 6 anode wire  
 382 planes crossed by 7 copper strips cathode panels in a gas volume. The  $r$  coordinate is provided  
 383 by the copper strips, while  $\phi$  coordinate comes from the anode wires, giving a two dimensional  
 384 position measurement. There are six layers of RPC in the barrel muon system and one layer into  
 385 each of the first three stations of the end cap. They are made from two high resistive plastic  
 386 plates with an applied voltage and separated by a gas volume. Read out strips mounted on top  
 387 of the plastic plates detect the signal generated by a muon passing through the gas volume. The  
 388 RPC provides a fast response with a time resolution of 1 ns and covers a range of  $|\eta| < 1.8$   
 389 (Run I configuration).

391 During the LS1, the muon system underwent major upgrades [50, 51]. In the fourth station  
 392 of each end cap, the outermost rings of CSC and RPC chambers were completed, providing an

393 angular region of  $1.2 < |\eta| < 1.8$  for Run II, increasing the system redundancy, and allowing  
 394 tighter cuts on the trigger quality. In order to reduce the environmental noise, outer yoke discs  
 395 have been placed on both sides for the end caps. At the innermost rings of the first station, the  
 396 CSC has been upgraded by refurbishing the readout electronics to make use of the full detector  
 397 granularity instead of groups of three (Run I).

398 The muon system provides triggering on muons, identifying muons and improves the momentum  
 399 measurement and charge determination of high  $p_T$  muons. On top of the muon system,  
 400 the muon energy is deposited in the electromagnetic calorimeter, the hadronic calorimeter, and  
 401 outer calorimeter. The high magnetic field enables an efficient first level trigger and allows a  
 402 good momentum resolution of  $\Delta p/p \approx 1\%$  for a  $p_T$  of 100 GeV and  $\approx 10\%$  for a  $p_T$  of 1 TeV  
 403 (FIXME). There is an efficient muon measurement up to  $|\eta| < 2.4$ .

#### 404 Muon reconstruction

405 The muon reconstruction[52] has three subdivision: local reconstruction, regional reconstruction  
 406 and global reconstruction. The local reconstruction is performed on individual detector elements  
 407 such as strip and pixel hits in the inner tracking system, and muon hits and/or segments  
 408 on the muon chambers. Independent tracks are reconstructed in the inner tracker - called  
 409 tracker track - and in the muon system, called standalone tracks. Based on these tracks,  
 410 two reconstructions are considered. The outside-in approach is referred to as Global Muon  
 411 reconstruction. For each standalone track, a tracker track is found by comparing the parameters  
 412 of the two tracks propagated onto a common surface. Combining the hits from the tracker  
 413 track and the standalone track, gives a fit via the Kalman filter technique [53, 54] for a global  
 414 muon track. The second approach is an inside-out reconstruction, creating tracker muons. All  
 415 candidate tracker tracks are extrapolated to the muon system taking into account the magnetic  
 416 field, the average expected energy losses, and multiple Coulomb scattering in the detector  
 417 material. When at least one muon segment - DT or CSC hits - matches the extrapolated track,  
 418 the corresponding tracker track is indicated as a tracker muon.

419 For low transverse momenta ( $p_T \lesssim 5$  GeV), the tracker muon reconstruction is more efficient  
 420 than the global muon approach. This is due to the fact that tracker muons only require a  
 421 single muon segment in muon system, while the global muon approach requires typically  
 422 segments in at least two muon stations. The global muon approach typically improves the  
 423 tracker reconstruction for  $p_T \gtrsim 200$  GeV.

#### 424 2.2.2.2 Solenoid

425 Making use of the knowledge of previous experiments of ALEPH and DELPHI at LEP and H1  
 426 at HERA, CMS choose for a large super conducting solenoid with a length of 12.9 m and  
 427 a inner bore of 5.9 m[45]. With 2 168 turns, a current of 19.5 kA and a total energy of 2.7  
 428 GJ, a large bending power can be obtained for a modestly-sized solenoid. In order to ensure a  
 429 good momentum resolution in the forward regions, a favourable length/radius was necessary.  
 430 In Figure 2.9, a photo of the CMS solenoid is given.

431 The solenoid uses a high-purity aluminium stabilised conductor with indirect cooling from  
 432 liquid helium, together with fully epoxy impregnation. A four-layer winding is implemented that

433 can withstand an outward pressure of 64 atm. The NbTi cable is co-extruded by pure aluminium  
 434 that acts as a thermal stabilizer and has an aluminium alloy for mechanical reinforcement. The  
 435 return of the magnetic field is done by five wheels, noted by YB in [Figure 2.7](#).

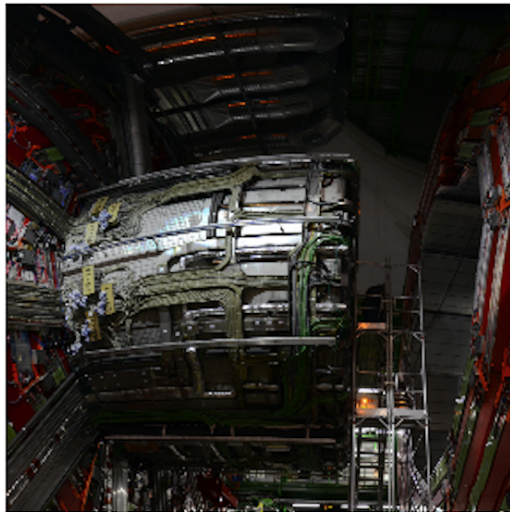


**Figure 2.9:** CMS solenoid during the long shutdown in 2013.

#### 436 2.2.2.3 Hadronic calorimeter

437 The hadronic calorimeter (HCAL) is dedicated to precisely measure the energy of charged and  
 438 neutral hadrons via a succession of absorbers and scintillators. This makes it crucial for physics  
 439 analyses with hadronic jets or missing transverse energy. The HCAL extends between 1.77  
 440  $< r < 2.95$  m where  $r$  is the radius in the transverse plane with respect to the beam. Due  
 441 to space limitations, the HCAL needs to be as small as possible and is made from materials  
 442 with short interaction lengths - the length needed for absorbing 36.7% of the hadrons. The  
 443 quality of the energy measurements is dependant on the fraction of the hadronic shower that  
 444 can be detected. Therefore, the HCAL barrel (HB) inside the solenoid is reinforced by an outer  
 445 hadronic calorimeter between the solenoid and muon detectors (HO, see [Figure 2.10](#)), using the  
 446 solenoid as extra absorber. This increases the thickness to 12 interaction lengths. Furthermore,  
 447 it should be as hermetic as possible and extend to large pseudo rapidity values. The HB and HO  
 448 provide measurements for  $|\eta| < 1.3$ , while an end cap on each side (HE,  $1.3 < |\eta| < 3$ ) and a  
 449 forward calorimeter (HF,  $|\eta| < 5.2$ ) extend the pseudo rapidity range.

450 The HB is made of 16 absorber plates where most of them are built from brass and others  
 451 are made from stainless steel and is about five to ten interaction lengths thick. The HE is also  
 452 composed of brass absorber plates and has a thickness corresponding to approximately ten  
 453 interaction lengths. The HF experiences intense particle fluxes with an energy of 760 GeV  
 454 deposited on average in a proton interaction at a center of mass of 14 TeV, compared to 100  
 455 GeV in the rest of the detector. Therefore, these are Cherenkov light detectors made of radiation  
 456 hard quartz fibers. The main causes of such large energy events are high energy muons, cosmic  
 457 particles and charged particles from late showering hadrons. During Run I, it became clear that  
 458 the glass windows of the PMTs had to be replaced which was done during LS1 [55]

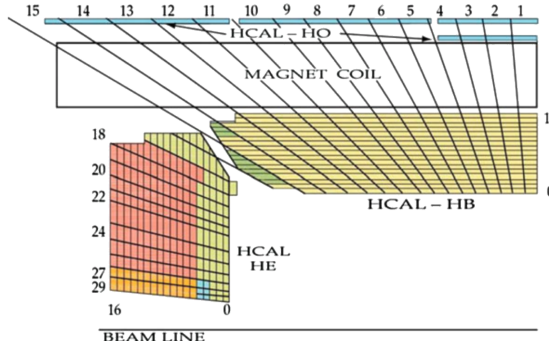


**Figure 2.10:** Tower segmentation for one quarter of the HCAL displayed in the  $r z$  plane[33].

#### 459 2.2.2.4 Electromagnetic calorimeter

460 The electromagnetic calorimeter (ECAL) is designed to measure the energy of photons and  
 461 electrons and covers  $|\eta| < 3$ . It is an hermetic, homogeneous detector and consists of 75 848  
 462 lead tungstate ( $\text{PbWO}_4$ ) crystals. These crystals have a fast response time - 80% of the light  
 463 is emitted within 25 ns - and are radiation hard. The electromagnetic showers produced by  
 464 passing electrons or photons ionize the crystal atoms which emit a blue-green scintillation light,  
 465 that is collected by silicon avalanche photodiodes (APDs) in the barrel and vacuum phototriodes  
 466 (VPTs) in the end caps. The crystals and the APD response is sensitive to temperature changes  
 467 and require a stable temperature.

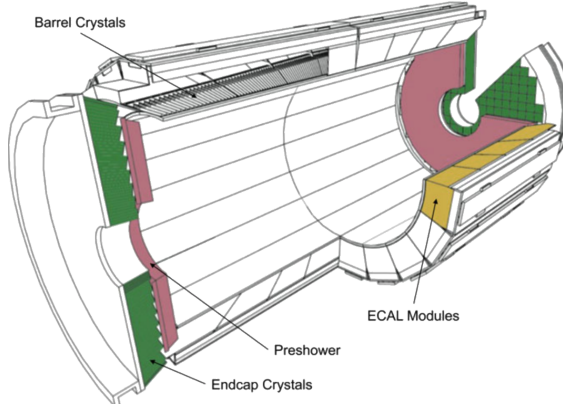


**Figure 2.11:** Schematic cross section of the electromagnetic calorimeter[33].

468 There are three regions: a central barrel (EB), a endcap region (EE) and a preshower (ES)  
 469 (Figure 2.11). The EB has an inner radius of 129 cm and corresponds to a pseudo rapidity  
 470 of  $0 < |\eta| < 1.479$ . At a distance of 314 cm from the vertex and covering a pseudo rapidity  
 471 of  $1.479 < |\eta| < 3.0$ , are the EE. They consist of semi-circular aluminium plates from which  
 472 structural units of  $5 \times 5$  crystals (super crystals) are supported. The ES is placed in front of  
 473 the crystal calorimeter over the end cap pseudo rapidity range with two planes of silicon strip  
 474 detectors as active elements.

The electromagnetic shower will typically involve more than one channel. More than 90% of

the energy of a 35 GeV electron or photon is contained in a  $5 \times 5$  matrix of crystals. Therefore, a clustering algorithm is performed in order to associate the energy deposits to the particles impinging the calorimeter. The achieved precision[56] for the barrel is  $2.10^{-3}$  rad in  $\phi$  and  $10^{-3}$  in  $\eta$ . For the end caps this is  $5.10^{-3}$  rad in  $\phi$  and  $2.10^{-3}$  in  $\eta$ . The energy is reconstructed by a super cluster algorithm, taking into account energy radiated via bremsstrahlung or conversion:

$$E_{e/\gamma} = GF_{e/\gamma} \sum_{i \in \text{cluster}} S_i(t) V C_i A_i, \quad (2.5)$$

where  $G$  is the absolute energy scale in GeV/ADC,  $F$  the energy containment corrections (depends on type of particle, its energy and pseudo rapidity, eg shower leakage and bremsstrahlung losses for electrons),  $S(t)$  the relative channel variation with time,  $C$  the relative channel response and  $A$  the amplitude in ADC counts. The energy resolution is given by

$$\frac{\sigma(E)}{E} = \frac{2.8\%}{\sqrt{E}} \oplus \frac{0.128}{E(\text{GeV})} \oplus 0.3\%, \quad (2.6)$$

475 in the absence of a magnetic field, where the contributions come from the stochastic, noise and  
 476 constant terms respectively. The dominating term is the constant term ( $E_{\text{shower}} \approx 100\text{GeV}$ ) and  
 477 thus the performance is highly dependent on the quality of calibration and monitoring .

478 In Run I, the energy reconstruction happened via a weighted sum of the digitized samples[57].  
 479 For Run II however, the reconstruction had to be made more resistant for out of time pile up  
 480 and a multi-fit approach has been set in to place. In this approach, the pulse shape is modelled  
 481 as a sum of one in-time pulse plus the out of time pulses [56]. The energy resolution is less  
 482 than 2% in the central barrel region and 2-5 % elsewhere.

#### 483 2.2.2.5 Inner tracking system and operations

484 The tracking system (tracker) [58] is the detecting unit closest to the point of interaction.  
 485 Responsible for the reconstruction of trajectories from charged particles with  $|\eta| < 2.5$  that are  
 486 bent by the magnetic field, it provides a measurement of the momentum. The tracker is also  
 487 responsible for the determination of the interaction point or vertex. It should be able to provide  
 488 high granularity as well as speed, and be able to endure high radiation. For this reason, the  
 489 CMS collaboration choose silicon detector technology.

490 The tracking system consists of a cylinder of 5.8 m long and 2.5 m in diameter. It is immersed  
 491 in a co-axial magnetic field of 3.8 T due to the solenoid. As shown Figure 2.12, the tracker  
 492 is built up from a large silicon strip tracker with a small silicon pixel inside. The inner region,  
 493 pixel ( $4.4 < r < 10.2$  cm), gets the highest flux of particles. Therefore, pixel silicon sensors  
 494 of  $100 \times 150$   $\mu\text{m}$  area used. It consists of three cylindrical barrels that are complemented by  
 495 two discs of pixel modules at each side. The silicon strip tracker ( $20 < r < 116$  cm ) has three  
 496 subdivisions. The Tracker Inner Barrel and Discs (TIB, TID, see Figure 2.14) are composed  
 497 of four barrel layers accompanied by three discs at each end. The outer part of the tracker -  
 498 Tracker Outer Barrel (TOB) - consists of 6 barrel layers. In the outer discs, there are nine discs  
 499 of silicon sensors, referred to as Tracker End Caps (TEC).

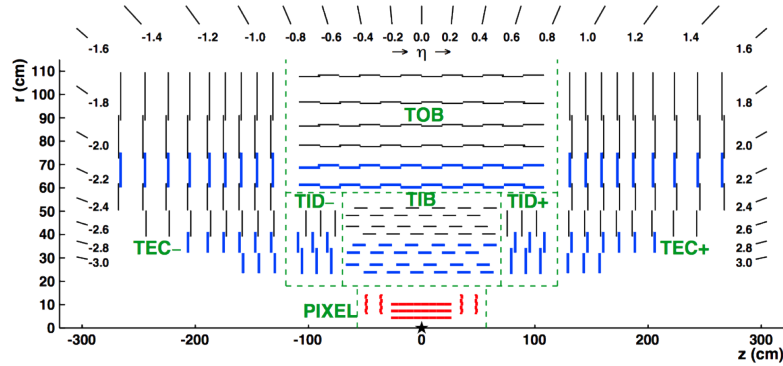


**Figure 2.12:** Schematic cross section of the top half of the CMS tracking system in the  $r$ - $z$  plane. The centre of tracker is shown with a star and corresponds to the approximate position of the proton collision point. The green dashed lines are an indication for each named tracker subsystem. The strip tracker modules that provide two-dimensional hits are shown by thin, black lines, while those able to reconstruct three-dimensional hit positions are shown by thick, blue lines. The pixel modules, shown in red, also provide three-dimensional hits. [44]

500 The pixel, shown in Figure 2.13 has 1440 modules that cover an area of about  $1 \text{ m}^2$  and have  
 501 66 million pixels. It provides a three-dimensional position measurement of the hits arising from  
 502 the interaction from charged particles with the sensors. In transverse coordinate ( $r\phi$ ), the hit  
 503 position resolution is about  $10 \mu\text{m}$ , while  $20\text{-}40 \mu\text{m}$  is obtained in the longitudinal coordinate  
 504 ( $z$ ). The sensor plane position provides the third coordinate. The silicon strip trackers consists  
 505 of 15 148 single sided modules placed in the TIB, TID and the first four rings of the TEC.  
 506 They provide 9.3 million readout channels. In the TOB and the outer three rings of the TEC,  
 507 double sided modules are used. These modules are constructed from two back-to-back single  
 508 sided modules, where one module is rotated through a stereo angle. This covers an active area  
 509 of about  $198 \text{ m}^2$ . The TIB and TID provide position measurements in  $r\phi$  with a resolution  
 510 of approximately  $13\text{-}38 \mu\text{m}$ , while the TOB provides a resolution of about  $18\text{-}47 \mu\text{m}$ . The  
 511 resolution in the  $z$  direction is approximately  $230 \mu\text{m}$  in the TIB/TID and  $530 \mu\text{m}$  in the TOB.  
 512 To allow overlay and avoid gaps in acceptance, each module is shifted slightly in  $r$  or  $z$  with  
 513 respect to its neighbouring modules within a layer. With this detector lay out, at least nine  
 514 points per charged particle trajectory can be measured in an  $|\eta|$  range up to 2.4.

During the first data taking period of the LHC (2010 to 2013), the tracker operated at  $+4^\circ\text{C}$ . With the higher LHC beam intensities from 2015 onwards, the tracker needs to be operated at much lower temperatures. This is due to the fact with intense irradiation, the doping concentration changes, the leakage current increases proportional to the fluence and the charge collection efficiency decreases due to charge trapping. Mostly the leakage current ( $I$ ) is affected by the temperature change:

$$I \propto T^2 e^{-\frac{E_g}{2kT}}, \quad (2.7)$$

515 where  $T$  is the operating temperature,  $E_g$  the band gap and  $k$  the Boltzmann constant. There is  
 516 approximately a factor 15 between the leakage currents at room temperatures and at  $-10^\circ\text{C}$ .



**Figure 2.13:** The pixel barrel being re-installed after the Long Shutdown in 2015, around the beam pipe at CMS[59]

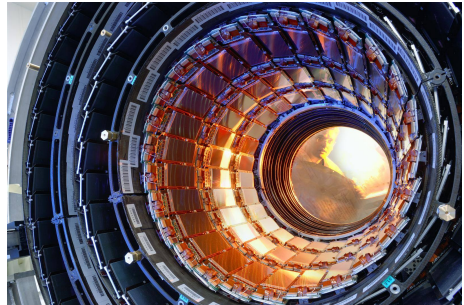


**Figure 2.14:** First half of the inner tracker barrel, consisting of three layers of silicon modules.[60]

517 During the LS1, the CMS cooling plant was refurbished[61](Figure 2.16) and the fluorocarbon  
 518 cooling system overhauled. To help to suppress the humidity inside the tracker, new methods  
 519 for vapour sealing and insulation were applied (Figure 2.15). Furthermore, several hundred  
 520 high-precision sensors are used to monitor the humidity and temperature. In order to get as  
 521 dry air as possible, a new dry-gas plant provides eight times more dry gas (air or nitrogen)  
 522 than during the first run, and allows regulation if the flow. As final addition, the cooling  
 523 bundles outside the tracker are equipped with heater wires and temperature sensors in order to  
 524 maintain safe operations above the cavern dew point For the data taking in 2015-2016, the  
 525 tracker operated at  $-15^{\circ}\text{C}$ .

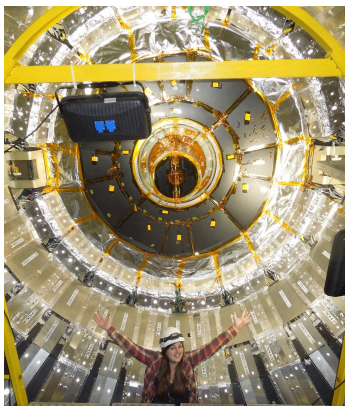


**Figure 2.15:** Tracker bulkhead being put into closed state with insulation pieces installed during an early trial in fall 2013



**Figure 2.16:** New Tracker high-capacity dry-gas plant with membrane separation system[48]

## 526 Track reconstruction

527 An iterative tracking algorithm is responsible for the reconstruction of the tracks made by  
 528 charged particles in the inner tracking system. Each iteration consists of four steps[45]: the  
 529 track-seed generation, the pattern recognition algorithm, removal of track-hit ambiguities and

530 a final track fit.

531 The seed generation is the first step. It consists of finding reconstructed hits that are usable  
 532 for seeding the subsequent track-finding algorithm. They are identified from a group of at  
 533 least three reconstructed hits in the tracker, or from a pair of hits while requiring the origin  
 534 of the track segment to be compatible with the nominal beam-collision point. Since the pixel  
 535 has a higher granularity compared to the strip tracker, its seed generation efficiency is higher.  
 536 The overall efficiency exceeds 99%. The second step of each iteration, the pattern recognition  
 537 algorithm, uses the seeds as a starting point for a Kalman filter method [53, 54]. This algorithm  
 538 extrapolates the seed trajectory towards the next tracker layer taking into account the magnetic  
 539 field and multiple scattering effects. The track parameters are updated when a compatible hit  
 540 in the next layer is found. This procedure continues until the outermost layer is reached. Since  
 541 the Kalman filter method can result in multiple tracks associated to the same seed, or different  
 542 tracks sharing the same hits, a removal of ambiguities is necessary. This ambiguity resolving is  
 543 done by removing tracks that are sharing too many hits from the list of track candidates. The  
 544 tracks with highest number of hits or with the lowest  $\chi^2$  if the track fit is kept. The updated  
 545 track parameters are then refitted using the Kalman filter method, where all hits found in the  
 546 pattern recognition step are taken into account. The fit is done twice - once outwards from the  
 547 beam line towards the calorimeters, and inwards from the outermost track hit to the beam line  
 548 -, improving the estimation of the track parameters.

549 All hits that are unambiguously associated to the final track are removed from the list of  
 550 available hits. In order to associate the remaining hits, the procedure is repeated with looser  
 551 track reconstruction criteria. The use of the iterative track reconstruction procedure has a  
 552 high track finding efficiency, where the fake track reconstruction rate is negligible. For muons,  
 553 this results in a global track reconstruction efficiency exceeding 98%, and 75-98% for charged  
 554 hadrons.

## 555 Primary vertex reconstruction

556 The primary vertex reconstruction should be able to measure the location of all proton interaction  
 557 vertices in each event: the signal vertex and all vertices from pile up events. It consists of a vertex  
 558 finding and a vertex fitting algorithm and happens in three steps. Tracks are selected to be  
 559 consistent with being produced promptly in the primary interaction by imposing requirements  
 560 on the track parameters[58] By grouping reconstructed tracks according to the z coordinate of  
 561 their closest approach to the beam line, vertices for all interaction in the same beam crossing  
 562 are found, at CMS this is done by a deterministic annealing algorithm [62] . On top of this,  
 563 a vertex fitting algorithm like the Adaptive Vertex fitter [63], is performed. This creates the  
 564 three-dimensional primary-vertex position. With this fit, the contribution from long-lived hadron  
 565 decays is reduced by down weighting the tracks with a larger distance to the vertex. The primary  
 566 vertex corresponding to the highest sum of squared track transverse momenta is noted as the  
 567 point of the main interaction. The resolution on the primary vertex is about 14  $\mu\text{m}$  in  $r\phi$  and  
 568 about 19  $\mu\text{m}$  in the z direction for primary vertices with the sum of the track  $p_T > 100$  GeV  
 569 for 2016 data taking.

570 **2.2.3 Data acquisition**

571 At a design luminosity of  $10^{34} \text{ 1/(m}^2 \text{ s)}$ , the proton interaction rate exceeds 1 GHz. This makes  
 572 it impossible for the CMS experiment to store all the data generated. For this, a two level trigger  
 573 system has been put in place. The first level (Level-1) is a custom hardware system, while a  
 574 second level (HLT) is software based running on a large farm of computers. In run II, with the  
 575 increase in centre of mass energy and a higher luminosity, a larger number of simultaneous  
 576 inelastic collisions per crossing is expected with respect to run I. For this, the CMS Level-1 has  
 577 been upgraded [64].

578 **CMS Level-1 trigger**

579 The Level-1 trigger has to be a flexible, maintainable system, capable of adapting to the evolving  
 580 physics programme of CMS [65]. Its output rate is restricted to 100 kHz imposed by the CMS  
 581 readout electronics. It is implemented by custom hardware and selects events containing candi-  
 582 date objects - eg ionization deposits consistent with a muon, or energy clusters corresponding  
 583 to an electron / photon / tau lepton / missing transverse energy / jet. Collisions with large  
 584 momenta can be selected by using scalar sum of the transverse momenta of the jets.

585 By buffering the raw data from the CMS subdetectors in front-end drivers, the level-1 trigger  
 586 has a pipeline memory of 3.2  $\mu\text{s}$  to decide whether to keep an event or reject it. The trigger  
 587 primitives (TP) from the calorimeters and muon detectors are processed in several steps and  
 588 combined into a global trigger. This information is then combined with the input from the other  
 589 subsystems for the HLT. The separate inputs are synchronized to each other and the LHC orbit  
 590 clock and sent to the global trigger module. Here, level-1 trigger algorithms are performed  
 591 within 1  $\mu\text{s}$  to decide whether to keep the event.

592 For run II, all hardware, software, databases and the timing control system have been replaced.  
 593 The main changes are that the muon system now uses the redundancy of three muon detector  
 594 system earlier to make a high resolution muon trigger. Other upgrades are that the calorimeter  
 595 system isn't bound any more for streaming data the data and the global trigger has more level-1  
 596 trigger algorithms.

597 **CMS HLT trigger**

598 The HLT is an array of commercially available computers with programmable menu that has  
 599 output rate of on average 400 Hz for off-line event storage. The data processing is based on a  
 600 HLT path. This is a set of algorithmic steps to reconstruct objects and make selections on them.  
 601 Here, the information of all sub detectors can be used to perform algorithms on higher level  
 602 reconstructed objects.

603 **2.2.4 CMS computing model**

604 The selected data is stored, processed and dispersed via the Worldwide Large Hadron Collider  
 605 GRID (WLCG)[66, 67]. This has a tiered structure that function as a single, coherent system:

606 At CERN, a single Tier-0 is located. The raw data collected by CMS is archived here, and  
 607 a first reconstruction of the data is done. This data is then already in a file format usable for

608 physics analysis. Furthermore, it is able to reprocess data when new calibrations are made  
609 available. The Tier-0 site distributes this data to a total of seven Tier-1 centres. They carry out  
610 data reprocessing and store real data as well as simulated data. The Tier-1 further distribute  
611 the data to over 50 Tier-2 centres. These make the data accessible for physics analysis and are  
612 also being used for the production of simulated data. The data is made accessible for physicists  
613 around the world.



# Event generation, simulation and reconstruction

3

614

## 615 **3.1 Collision event generation**

616 **3.1.1 Parton distribution functions and the hard interaction**

617 **3.1.2 Parton showering**

618 **3.1.3 Hadronisation and decay**

619 explanation of jets <https://profmattstrassler.com/articles-and-posts/particle-physics-basics/the-known-apparently-elementary-particles/jets-the-manifestation-of-quarks-and-gluons/>

621 **3.1.4 Underlying event**

622 **3.1.5 Event reconstruction and identification**

## 623 **3.2 Detector simulation**

## 624 **3.3 Physics object reconstruction and identification**

625 **3.3.1 The particle flow event reconstruction method**

626 **3.3.2 Identification of particles**

627 **3.3.2.1 Muon reco and ID**

628 **3.3.2.2 Electron reco and ID**

629 **3.3.2.3 Jet reco and ID of b quarks**

630 **3.3.2.4 Missing transverse energy reconstruction**

631 **3.3.3 Calibrations and corrections**



# The search for FCNC involving a top quark and a Z boson

4

633 **4.1 Model assumptions**

634 **4.2 Data and simulation**

635 **4.2.1 Standard Model Background simulation**

636 **4.2.2 FCNC signal simulation**

637 In this thesis, two scenarios are being studied: one being the top-up interactions and the second  
638 one being top-charm interactions. For a given flavour of light quark  $q$ , all left-handed chiral  
639 parameters were set to zero and all right-handed set to one

640 **4.2.3 Trigger requirements**

641 **4.3 Baseline event selection**

642 **4.4 Data driven background estimation**

643 **4.5 Regions and channels**

644 **4.6 Construction of template distributions**

645 **4.7 Systematic uncertainties**

646 **4.8 Limit setting procedure**

647 **4.9 Result and discussion**



## Conclusion and outlook

5

---



# Bibliography

---

- 650 [1] MICHAEL E PESKIN and DANIEL V SCHROEDER: **An introduction to quantum field**  
 651 **theory; 1995 ed.** Includes exercises. Boulder, CO: Westview, 1995. URL: <https://cds.cern.ch/record/257493> (see pp. 1, 5).
- 653 [2] NADIA ROBOTTI: **The discovery of the electron: I.** In: *European Journal of Physics*, **18**:3  
 654 (1997), p. 133. URL: <http://stacks.iop.org/0143-0807/18/i=3/a=002> (see p. 2).
- 655 [3] C. PATRIGNANI et al.: **Review of Particle Physics.** In: *Chin. Phys.*, **C40**:10 (2016),  
 656 p. 100001. DOI: [10.1088/1674-1137/40/10/100001](https://doi.org/10.1088/1674-1137/40/10/100001) (see pp. 2, 6).
- 657 [4] S. ABACHI et al.: **Observation of the top quark.** In: *Phys. Rev. Lett.*, **74**: (1995),  
 658 pp. 2632–2637. DOI: [10.1103/PhysRevLett.74.2632](https://doi.org/10.1103/PhysRevLett.74.2632). arXiv: [hep-ex/9503003](https://arxiv.org/abs/hep-ex/9503003) [hep-ex]  
 659 (see p. 2).
- 660 [5] F. ABE et al.: **Observation of top quark production in  $\bar{p}p$  collisions.** In: *Phys. Rev.*  
 661 *Lett.*, **74**: (1995), pp. 2626–2631. DOI: [10.1103/PhysRevLett.74.2626](https://doi.org/10.1103/PhysRevLett.74.2626). arXiv: [hep-ex/9503002](https://arxiv.org/abs/hep-ex/9503002) [hep-ex] (see p. 2).
- 663 [6] SERGUEI CHATRHYAN et al.: **Observation of a new boson at a mass of 125 GeV with**  
 664 **the CMS experiment at the LHC.** In: *Phys. Lett.*, **B716**: (2012), pp. 30–61. DOI:  
 665 [10.1016/j.physletb.2012.08.021](https://doi.org/10.1016/j.physletb.2012.08.021). arXiv: [1207.7235](https://arxiv.org/abs/1207.7235) [hep-ex] (see pp. 2, 13).
- 666 [7] GEORGES AAD et al.: **Observation of a new particle in the search for the Standard**  
 667 **Model Higgs boson with the ATLAS detector at the LHC.** In: *Phys. Lett.*, **B716**:  
 668 (2012), pp. 1–29. DOI: [10.1016/j.physletb.2012.08.020](https://doi.org/10.1016/j.physletb.2012.08.020). arXiv: [1207.7214](https://arxiv.org/abs/1207.7214) [hep-ex]  
 669 (see pp. 2, 13).
- 670 [8] PATRICK KOPPENBURG and SEBASTIEN DESCOTES-GENON: **The CKM Parameters.** In:  
 671 (2017). arXiv: [1702.08834](https://arxiv.org/abs/1702.08834) [hep-ex] (see p. 6).
- 672 [9] J. A. AGUILAR-SAAVEDRA: **Top flavor-changing neutral interactions: Theoretical ex-**  
 673 **pectations and experimental detection.** In: *Acta Phys. Polon.*, **B35**: (2004), pp. 2695–  
 674 2710. arXiv: [hep-ph/0409342](https://arxiv.org/abs/hep-ph/0409342) [hep-ph] (see pp. 6, 8).
- 675 [10] YORIKIYO NAGASHIMA: **Beyond the standard model of elementary particle physics.**  
 676 Weinheim, Germany: Wiley-VCH Verlag, 2014. URL: [http://www-spires.fnal.gov/  
 677 spires/find/books/www?cl=QC793.2.N34::2014](http://www-spires.fnal.gov/spires/find/books/www?cl=QC793.2.N34::2014) (see p. 6).
- 678 [11] A. D. SAKHAROV: **Violation of CP Invariance, c Asymmetry, and Baryon Asymmetry of**  
 679 **the Universe.** In: *Pisma Zh. Eksp. Teor. Fiz.*, **5**: (1967). [Usp. Fiz. Nauk 161, 61 (1991)],  
 680 pp. 32–35. DOI: [10.1070/PU1991v034n05ABEH002497](https://doi.org/10.1070/PU1991v034n05ABEH002497) (see p. 7).

- [681] [12] T. ET AL. AALTONEN: **Search for the Flavor-Changing Neutral-Current Decay  $t \rightarrow Zq$  in  $p\bar{p}$  Collisions at  $\sqrt{s} = 1.96$  TeV.** In: *Phys. Rev. Lett.*, **101**: (19 Nov. 2008), p. 192002. doi: [10.1103/PhysRevLett.101.192002](https://doi.org/10.1103/PhysRevLett.101.192002) (see p. 8).
- [684] [13] VICTOR MUKHAMEDOVICH ABAZOV et al.: **Search for flavor changing neutral currents via quark-gluon couplings in single top quark production using  $2.3 \text{ fb}^{-1}$  of  $p\bar{p}$  collisions.** In: *Phys. Lett.*, **B693**: (2010), pp. 81–87. doi: [10.1016/j.physletb.2010.08.011](https://doi.org/10.1016/j.physletb.2010.08.011). arXiv: [1006.3575 \[hep-ex\]](https://arxiv.org/abs/1006.3575) (see p. 8).
- [688] [14] GEORGES AAD et al.: **Search for flavour-changing neutral current top-quark decays to  $qZ$  in  $pp$  collision data collected with the ATLAS detector at  $\sqrt{s} = 8$  TeV.** In: *Eur. Phys. J.*, **C76**:1 (2016), p. 12. doi: [10.1140/epjc/s10052-015-3851-5](https://doi.org/10.1140/epjc/s10052-015-3851-5). arXiv: [1508.05796 \[hep-ex\]](https://arxiv.org/abs/1508.05796) (see p. 8).
- [692] [15] GEORGES AAD et al.: **Search for single top-quark production via flavour-changing neutral currents at 8 TeV with the ATLAS detector.** In: *Eur. Phys. J.*, **C76**:2 (2016), p. 55. doi: [10.1140/epjc/s10052-016-3876-4](https://doi.org/10.1140/epjc/s10052-016-3876-4). arXiv: [1509.00294 \[hep-ex\]](https://arxiv.org/abs/1509.00294) (see p. 8).
- [695] [16] ALBERT M SIRUNYAN et al.: **Search for associated production of a Z boson with a single top quark and for tZ flavour-changing interactions in pp collisions at  $\sqrt{s} = 8$  TeV.** In: (2017). arXiv: [1702.01404 \[hep-ex\]](https://arxiv.org/abs/1702.01404) (see p. 8).
- [698] [17] SERGUEI CHATRCHYAN et al.: **Search for Flavor-Changing Neutral Currents in Top-Quark Decays  $t \rightarrow Zq$  in  $pp$  Collisions at  $\sqrt{s} = 8$  TeV.** In: *Phys. Rev. Lett.*, **112**:17 (2014), p. 171802. doi: [10.1103/PhysRevLett.112.171802](https://doi.org/10.1103/PhysRevLett.112.171802). arXiv: [1312.4194 \[hep-ex\]](https://arxiv.org/abs/1312.4194) (see p. 8).
- [702] [18] VARDAN KHACHATRYAN et al.: **Search for anomalous single top quark production in association with a photon in pp collisions at  $\sqrt{s} = 8$  TeV.** In: *JHEP*, **04**: (2016), p. 035. doi: [10.1007/JHEP04\(2016\)035](https://doi.org/10.1007/JHEP04(2016)035). arXiv: [1511.03951 \[hep-ex\]](https://arxiv.org/abs/1511.03951) (see p. 8).
- [705] [19] J. A. AGUILAR-SAAVEDRA: **A Minimal set of top anomalous couplings.** In: *Nucl. Phys.*, **B812**: (2009), pp. 181–204. doi: [10.1016/j.nuclphysb.2008.12.012](https://doi.org/10.1016/j.nuclphysb.2008.12.012). arXiv: [0811.3842 \[hep-ph\]](https://arxiv.org/abs/0811.3842) (see p. 8).
- [708] [20] J. A. AGUILAR-SAAVEDRA: **A Minimal set of top-Higgs anomalous couplings.** In: *Nucl. Phys.*, **B821**: (2009), pp. 215–227. doi: [10.1016/j.nuclphysb.2009.06.022](https://doi.org/10.1016/j.nuclphysb.2009.06.022). arXiv: [0904.2387 \[hep-ph\]](https://arxiv.org/abs/0904.2387) (see p. 8).
- [711] [21] M. BENEKE et al.: **Top quark physics.** In: *1999 CERN Workshop on standard model physics (and more) at the LHC, CERN, Geneva, Switzerland, 25-26 May: Proceedings.* 2000, pp. 419–529. arXiv: [hep-ph/0003033 \[hep-ph\]](https://arxiv.org/abs/hep-ph/0003033). URL: <http://weblib.cern.ch/abstract?CERN-TH-2000-100> (see p. 8).
- [715] [22] JUN GAO, CHONG SHENG LI, and HUA XING ZHU: **Top Quark Decay at Next-to-Next-to Leading Order in QCD.** In: *Phys. Rev. Lett.*, **110**:4 (2013), p. 042001. doi: [10.1103/PhysRevLett.110.042001](https://doi.org/10.1103/PhysRevLett.110.042001). arXiv: [1210.2808 \[hep-ph\]](https://arxiv.org/abs/1210.2808) (see p. 9).
- [718] [23] STEPHEN MYERS: **The LEP Collider, from design to approval and commissioning.** John Adams' Lecture. Delivered at CERN, 26 Nov 1990. Geneva: CERN, 1991. URL: <http://cds.cern.ch/record/226776> (see p. 13).

- 721 [24] STEPHEN HOLMES, RONALD S MOORE, and VLADIMIR SHILTSEV: **Overview of the Teva-**  
722 **tron collider complex: goals, operations and performance.** In: *Journal of Instrumenta-*  
723 *tion*, 6:08 (2011), T08001. URL: <http://stacks.iop.org/1748-0221/6/i=08/a=T08001>  
724 (see p. 13).
- 725 [25] R. BARATE et al.: **Search for the standard model Higgs boson at LEP.** In: *Phys. Lett.*,  
726 **B565:** (2003), pp. 61–75. DOI: [10.1016/S0370-2693\(03\)00614-2](https://doi.org/10.1016/S0370-2693(03)00614-2). arXiv: [hep-ex/0306033](https://arxiv.org/abs/hep-ex/0306033)  
727 [[hep-ex](#)] (see p. 13).
- 728 [26] KENNETH HERNER: **Higgs Boson Studies at the Tevatron.** In: *Nucl. Part. Phys. Proc.*,  
729 **273-275:** (2016), pp. 852–856. DOI: [10.1016/j.nuclphysbps.2015.09.131](https://doi.org/10.1016/j.nuclphysbps.2015.09.131) (see p. 13).
- 730 [27] ABDELHAK DJOUADI: **The Anatomy of electro-weak symmetry breaking. I: The Higgs**  
731 **boson in the standard model.** In: *Phys. Rept.*, 457: (2008), pp. 1–216. DOI: [10.1016/j.physrep.2007.10.004](https://doi.org/10.1016/j.physrep.2007.10.004). arXiv: [hep-ph/0503172](https://arxiv.org/abs/hep-ph/0503172) [[hep-ph](#)] (see p. 13).
- 733 [28] LYNDON EVANS and PHILIP BRYANT: **LHC Machine.** In: *Journal of Instrumentation*, 3:08  
734 (2008), S08001. URL: <http://stacks.iop.org/1748-0221/3/i=08/a=S08001> (see p. 13).
- 735 [29] THOMAS SVEN PETTERSSON and P LEFÈVRE: **The Large Hadron Collider: conceptual**  
736 **design.** Tech. rep. CERN-AC-95-05-LHC. Oct. 1995, p. 20 and 22. URL: <https://cds.cern.ch/record/291782> (see p. 13).
- 738 [30] JORG WENNINGER and EZIO TODESCO: **Large Hadron Collider momentum calibration**  
739 **and accuracy.** Tech. rep. CERN-ACC-2017-0007. Geneva: CERN, Feb. 2017. URL:  
740 <https://cds.cern.ch/record/2254678> (see p. 14).
- 741 [31] CINZIA DE MELIS: **The CERN accelerator complex. Complexe des accélérateurs du**  
742 **CERN.** In: (July 2016). General Photo. URL: <https://cds.cern.ch/record/2197559> (see  
743 p. 14).
- 744 [32] G. AAD et al.: **The ATLAS Experiment at the CERN Large Hadron Collider.** In: *JINST*,  
745 **3:** (2008), S08003. DOI: [10.1088/1748-0221/3/08/S08003](https://doi.org/10.1088/1748-0221/3/08/S08003) (see p. 14).
- 746 [33] S. CHATRCHYAN et al.: **The CMS Experiment at the CERN LHC.** In: *JINST*, 3: (2008),  
747 S08004. DOI: [10.1088/1748-0221/3/08/S08004](https://doi.org/10.1088/1748-0221/3/08/S08004) (see pp. 14, 23).
- 748 [34] K. AAMODT et al.: **The ALICE experiment at the CERN LHC.** In: *JINST*, 3: (2008),  
749 S08002. DOI: [10.1088/1748-0221/3/08/S08002](https://doi.org/10.1088/1748-0221/3/08/S08002) (see p. 14).
- 750 [35] A. AUGUSTO ALVES JR. et al.: **The LHCb Detector at the LHC.** In: *JINST*, 3: (2008),  
751 S08005. DOI: [10.1088/1748-0221/3/08/S08005](https://doi.org/10.1088/1748-0221/3/08/S08005) (see p. 14).
- 752 [36] M. BONGI et al.: **Astroparticle physics at LHC: The LHCf experiment ready for data**  
753 **taking.** In: *Nucl. Instrum. Meth.*, A612: (2010), pp. 451–454. DOI: [10.1016/j.nima.2009.08.039](https://doi.org/10.1016/j.nima.2009.08.039) (see p. 14).
- 755 [37] G. ANELLI et al.: **The TOTEM experiment at the CERN Large Hadron Collider.** In:  
756 *JINST*, 3: (2008), S08007. DOI: [10.1088/1748-0221/3/08/S08007](https://doi.org/10.1088/1748-0221/3/08/S08007) (see p. 14).
- 757 [38] B. ACHARYA et al.: **The Physics Programme Of The MoEDAL Experiment At The LHC.**  
758 In: *Int. J. Mod. Phys.*, A29: (2014), p. 1430050. DOI: [10.1142/S0217751X14300506](https://doi.org/10.1142/S0217751X14300506).  
759 arXiv: [1405.7662](https://arxiv.org/abs/1405.7662) [[hep-ph](#)] (see p. 15).
- 760 [39] BY JAMES GILLIES: **Luminosity? Why don't we just say collision rate?** In: (Mar. 2011).  
761 URL: <https://cds.cern.ch/record/1997001> (see p. 15).

- 762 [40] BY HARRIET JARLETT and HARRIET KIM JARLETT: **LHC pushes limits of performance.**  
 763 In: (Aug. 2016). URL: <http://cds.cern.ch/record/2212301> (see p. 15).
- 764 [41] OLIVER SIM BRÜNING, PAUL COLLIER, P LEBRUN, et al.: **LHC Design Report.** CERN Yellow  
 765 Reports: Monographs. Geneva: CERN, 2004. URL: <https://cds.cern.ch/record/782076>  
 766 (see p. 15).
- 767 [42] JEAN-LUC CARON: **Cross section of LHC dipole.. Dipole LHC: coupe transversale.**  
 768 AC Collection. Legacy of AC. Pictures from 1992 to 2002. May 1998. URL: <https://cds.cern.ch/record/841539> (see p. 16).
- 770 [43] **Technical proposal.** LHC Tech. Proposal. Cover title : CMS, the Compact Muon Solenoid  
 771 : technical proposal. Geneva: CERN, 1994. URL: <https://cds.cern.ch/record/290969>  
 772 (see p. 17).
- 773 [44] G. L. BAYATIAN et al.: **CMS physics: Technical design report.** In: (2006) (see pp. 17,  
 774 25).
- 775 [45] G L BAYATIAN, S CHATRCHYAN, G HMAYAKYAN, et al.: **CMS Physics: Technical Design**  
 776 **Report Volume 1: Detector Performance and Software.** Technical Design Report CMS.  
 777 There is an error on cover due to a technical problem for some items. Geneva: CERN,  
 778 2006. URL: <https://cds.cern.ch/record/922757> (see pp. 17, 21, 26).
- 779 [46] BY CIAN O'LUANAIGH: **LHC progresses towards higher intensities.** In: (Aug. 2015).  
 780 URL: <http://cds.cern.ch/record/2051986> (see p. 17).
- 781 [47] CMS COLLABORATION: **Detector Drawings.** CMS Collection. Mar. 2012. URL: <https://cds.cern.ch/record/1433717> (see p. 18).
- 783 [48] BY CORINNE PRALAVORIO and CORINNE PRALAVORIO: **Major work to ready the LHC**  
 784 **experiments for Run 2.** In: (May 2015). URL: <http://cds.cern.ch/record/2024977>  
 785 (see pp. 17, 26).
- 786 [49] S CHATRCHYAN, V KHACHATRYAN, A M SIRUNYAN, et al.: **Performance of the CMS Drift**  
 787 **Tube Chambers with Cosmic Rays.** In: *J. Instrum.*, 5:arXiv:0911.4855. CMS-CFT-  
 788 09-012 (Nov. 2009), T03015 . 47 p. URL: <http://cds.cern.ch/record/1223944> (see  
 789 pp. 19–20).
- 790 [50] LUIGI GUIDUCCI: **CMS muon system towards LHC Run 2 and beyond.** Tech. rep. CMS-  
 791 CR-2014-333. Geneva: CERN, Oct. 2014. URL: <https://cds.cern.ch/record/1966038>  
 792 (see p. 20).
- 793 [51] CARLO BATTILANA: **The CMS muon system status and upgrades for LHC run-2 and**  
 794 **performance of muon reconstruction with 13 TeV data.** Tech. rep. CMS-CR-2016-  
 795 437. Geneva: CERN, Dec. 2016. URL: <http://cds.cern.ch/record/2239185> (see  
 796 p. 20).
- 797 [52] SERGUEI CHATRCHYAN et al.: **Performance of CMS muon reconstruction in  $pp$  col-**  
 798 **lision events at  $\sqrt{s} = 7$  TeV.** In: *JINST*, 7: (2012), P10002. doi: [10.1088/1748-0221/7/10/P10002](https://doi.org/10.1088/1748-0221/7/10/P10002). arXiv: [1206.4071 \[physics.ins-det\]](https://arxiv.org/abs/1206.4071) (see p. 21).
- 800 [53] R. FRÜHWIRTH: **Application of Kalman filtering to track and vertex fitting.** In: *Nu-*  
 801 *clear Instruments and Methods in Physics Research Section A: Accelerators, Spectromet-*  
 802 *eters, Detectors and Associated Equipment*, 262:2 (1987), pp. 444–450. doi: [http://dx.doi.org/10.1016/0168-9002\(87\)90887-4](https://doi.org/10.1016/0168-9002(87)90887-4) (see pp. 21, 27).

- 804 [54] PIERRE BILLOIR: **Progressive track recognition with a Kalman like fitting procedure.**  
805 In: *Comput. Phys. Commun.*, **57**: (1989), pp. 390–394. doi: [10.1016/0010-4655\(89\)90249-X](https://doi.org/10.1016/0010-4655(89)90249-X) (see pp. 21, 27).
- 807 [55] EMRAH TIRAS, BURAK BILKI, and YASAR ONEL: **Commissioning of CMS Forward Hadron  
808 Calorimeters with Upgraded Multi-anode PMTs and μTCA Readout.** In: (2016).  
809 arXiv: [1611.05232 \[physics.ins-det\]](https://arxiv.org/abs/1611.05232) (see p. 22).
- 810 [56] L. BRIANZA: **Precision crystal calorimetry in LHC Run II with the CMS ECAL.** In:  
811 *Journal of Instrumentation*, **12**:01 (2017), p. C01069. URL: <http://stacks.iop.org/1748-0221/12/i=01/a=C01069> (see p. 24).
- 813 [57] SERGUEI CHATRCHYAN et al.: **Energy Calibration and Resolution of the CMS Elec-  
814 tromagnetic Calorimeter in  $pp$  Collisions at  $\sqrt{s} = 7$  TeV.** In: *JINST*, **8**: (2013).  
815 [*JINST*8,9009(2013)], P09009. doi: [10.1088/1748-0221/8/09/P09009](https://doi.org/10.1088/1748-0221/8/09/P09009). arXiv: [1306.2016 \[hep-ex\]](https://arxiv.org/abs/1306.2016) (see p. 24).
- 817 [58] SERGUEI CHATRCHYAN, VARDAN KHACHATRYAN, ALBERT M SIRUNYAN, et al.: **Description  
818 and performance of track and primary-vertex reconstruction with the CMS tracker.**  
819 In: *J. Instrum.*, **9**:arXiv:1405.6569. CERN-PH-EP-2014-070. CMS-TRK-11-001 (May  
2014). Comments: Replaced with published version. Added journal reference and DOI,  
821 P10009. 80 p. URL: <http://cds.cern.ch/record/1704291> (see pp. 24, 27).
- 822 [59] BY CHRISTINE SUTTON: **Chronicles of CMS: the saga of LS1.** In: (May 2015). URL:  
823 <http://cds.cern.ch/record/2024986> (see p. 26).
- 824 [60] **A beautiful barrel for CMS.** In: (Mar. 2014). URL: <http://cds.cern.ch/record/1998635> (see p. 26).
- 826 [61] **Cool running for CMS tracker.** In: (Mar. 2014). URL: <http://cds.cern.ch/record/1998606> (see p. 26).
- 828 [62] K. ROSE: **Deterministic annealing for clustering, compression, classification, re-  
829 gression, and related optimization problems.** In: *Proceedings of the IEEE*, **86**:11 (Nov.  
830 1998), pp. 2210–2239. doi: [10.1109/5.726788](https://doi.org/10.1109/5.726788) (see p. 27).
- 831 [63] WOLFGANG WALTENBERGER: **Adaptive Vertex Reconstruction.** Tech. rep. CMS-NOTE-  
832 2008-033. Geneva: CERN, July 2008. URL: <https://cds.cern.ch/record/1166320> (see  
833 p. 27).
- 834 [64] L. CADAMURO: **The CMS Level-1 trigger system for LHC Run II.** In: *Journal of Instru-  
835 mentation*, **12**:03 (2017), p. C03021. URL: <http://stacks.iop.org/1748-0221/12/i=03/a=C03021> (see p. 28).
- 837 [65] VARDAN KHACHATRYAN et al.: **The CMS trigger system.** In: *JINST*, **12**:01 (2017),  
838 P01020. doi: [10.1088/1748-0221/12/01/P01020](https://doi.org/10.1088/1748-0221/12/01/P01020). arXiv: [1609.02366 \[physics.ins-det\]](https://arxiv.org/abs/1609.02366)  
839 (see p. 28).
- 840 [66] CLAUDIO GRANDI, DAVID STICKLAND, LUCAS TAYLOR, ACHILLE PETRILLI, and ALAIN HERVÉ:  
841 **CMS Computing Model: The "CMS Computing Model RTAG".** Tech. rep. CMS-NOTE-  
842 2004-031. CERN-LHCC-2004-035. LHCC-G-083. Geneva: CERN, Dec. 2004. URL:  
843 <http://cds.cern.ch/record/814248> (see p. 28).

- 844 [67] CHRISTOPH ECK, J KNOBLOCH, LESLIE ROBERTSON, et al.: **LHC computing Grid: Techni-**  
845 **cal Design Report. Version 1.06 (20 Jun 2005).** Technical Design Report LCG. Geneva:  
846 CERN, 2005. URL: <https://cds.cern.ch/record/840543> (see p. 28).